Journal of Power Sources 553 (2023) 232251

Contents lists available at ScienceDirect

Journal of Power Sources

journal homepage: www.elsevier.com/locate/jpowsour

Coordination flexibility as a high-throughput descriptor for identifying solid electrolytes with Li^+ sublattice disorder: A computational and experimental study

Yu-Ying Lin [a,c], Jiaxing Qu [b,1], William J. Gustafson [b,c], Po-Cheng Kung [a,c], Nachiket Shah [a,c], Samyukta Shrivastav [a,c], Elif Ertekin [b,c], Jessica A. Krogstad [a,c,*], Nicola H. Perry [a,c,*]

[a] Department of Materials Science and Engineering, University of Illinois Urbana-Champaign, Urbana, IL, USA
[b] Department of Mechanical Science and Engineering, University of Illinois Urbana-Champaign, Urbana IL, USA
[c] Materials Research Laboratory, University of Illinois Urbana-Champaign, Urbana, IL, USA

HIGHLIGHTS

- Funnel-like physical descriptor screening could identify new Li^+ conductors rapidly.
- Li_7BiO_6, $Li_2B_4O_7$ and fast ion conductors exhibited "proximal stoichiometry" feature.
- In-depth experimental/computational studies were performed on Li_7BiO_6, $Li_2B_4O_7$.
- "Proximal stoichiometry" feature could be associated with Li-sublattice disorder.
- Li_7BiO_6 could accept extrinsic Li interstitials; $Li_2B_4O_7$ was a line compound.

GRAPHICAL ABSTRACT

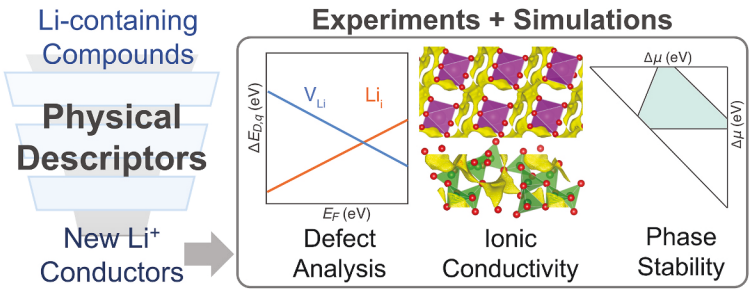

ARTICLE INFO

Keywords:
High-throughput descriptor
Li^+ solid electrolyte
Defect chemistry
Phase stability
Ionic conductivity

ABSTRACT

High-throughput descriptors are of interest for identifying new Li^+ conductors for all-solid-state batteries. Li-sublattice disorder is one feature commonly observed in superionic conductors but not explored as a descriptor, since defect thermodynamics are time-consuming to calculate and absent from large materials databases. To screen for this feature using a computationally cheap descriptor, we hypothesized that coordination flexibility – the ability of Li^+ to occupy sites with different bonding environments – a) correlates with ease of Li vacancy/interstitial formation and sublattice disorder, and b) exists in compounds having nearby phases with similar Li stoichiometry. Insertion of Li^+ interstitials may even trigger concerted transport. We applied "proximal stoichiometry" and other filters (e.g., bond-valence migration energy, Li–Li coordination number) to down-select compositions from Materials Project. We found that many superionic conductors satisfy the "proximal stoichiometry" filter, motivating exploration of our newly identified compositions - Li_7BiO_6, $Li_2B_4O_7$ - with similar characteristics. Computationally, relatively low Li vacancy/interstitial formation energies were found for both. Experimentally, Li_7BiO_6 exhibited increased ionic conductivity upon Li^+ insertion (via extrinsic doping), albeit without induced concerted transport. $Li_2B_4O_7$ behaved like a line compound. The "proximal stoichiometry"

* Corresponding authors. Department of Materials Science and Engineering and Materials Research Laboratory, University of Illinois Urbana-Champaign, Urbana, IL, USA.
E-mail addresses: jakrogst@illinois.edu (J.A. Krogstad), nhperry@illinois.edu (N.H. Perry).
[1] Co-first authorship or equivalent.

https://doi.org/10.1016/j.jpowsour.2022.232251
Received 8 July 2022; Received in revised form 26 September 2022; Accepted 12 October 2022
Available online 1 November 2022

feature correlates with facile Li vacancy/interstitial formation (intrinsic Li-sublattice disorder), but not directly with concerted transport.

1. Introduction

Effective use of renewable but intermittent energy sources and the need for portable power supplies has driven the rise in energy storage via Li-ion batteries in everything from electric vehicles to grid-level storage. In recent years, this technology has seen a transition from liquid to solid electrolytes to realize next-generation, high-energy-density storage systems: all-solid-state batteries (ASSB). As a crucial component in ASSB, inorganic solid electrolytes can offer significant improvements in safety, longevity, and performance. While a number of promising Li^+ conductors have been studied, practical issues such as poor air stability, high mechanical stiffness, poor interface stability, limited electrochemical stability window, and manufacturing and recycling challenges still limit their applications in full cells [1,2]. It is clear that the identification of new solid electrolyte materials is of vital importance to realize ASSB [3–8]. However, the search for such candidates often relies on experimental trial-and-error attempts. Systematic exploration of design rules for new solid electrolyte materials can ultimately increase the efficiency of electrolyte development.

One approach to accelerate the materials discovery process is through computational, data-driven screening. For example, many descriptors focusing on framework ion structures [9–11] have been applied to identify new ionic conductors; approaches based on statistical correlation analysis and machine learning [12–15] can also improve the predictive power of these structural descriptors. In this study, we focus on a relatively unexplored chemical descriptor: Li^+ sublattice disorder, which has been suggested to be a key feature for high ionic conductivity [16–23]. Such disorder can also be described as cation Frenkel defect disorder, as Li^+ vacancy/interstitial pairs exist when Li^+ ions occupy various crystallographic sites, compared to a reference structure with Li^+ ions in a regular array of identical crystallographic sites. As Li^+ transport often occurs via point defect migration in superionic conductors (SICs) [24], the ability to form Li^+ vacancies/interstitials can be thought of as a prerequisite for ionic conduction. Thus, one expects ion transport to benefit from low Li^+ vacancy/interstitial formation energies. However, defect formation energy calculations are computationally expensive; they are also not widely available in searchable databases, especially for new or underexplored compositions. For the above reasons, a computationally cheaper proxy is needed to predict compounds capable of hosting Li^+ sublattice disorder and accommodating defects.

To that end, we hypothesized that the presence of diverse Li^+ coordination geometries within the ground state of a family of compounds would indicate that such chemistries enable Li^+ to occupy sites with different coordination environments readily, leading to low Li^+ vacancy/interstitial formation energies and the possibility for Li^+ sublattice/positional disorder at finite temperatures. More specifically, we hypothesized that compounds that support coordination flexibility are those that have nearby stable phases with proximal Li stoichiometry: Li^+ ions in these proximal compounds are often coordinated differently. In short, we propose that this "proximal stoichiometry" feature may be used as a descriptor/proxy to identify Li-disorder-tolerant compounds as candidate good ionic conductors. Fig. 1 illustrates this hypothesis.

Furthermore, if high Li^+ interstitial populations could be supported (e.g., by extrinsic acceptor doping), because of low defect formation energies, concerted ion transport could potentially be triggered. This mechanism, in which multiple ions travel collectively with reduced overall migration barriers, was shown to be responsible for high ionic conductivity in many SICs [25–32]. The insertion of extra Li^+/Na^+ (or interstitials) was proposed as a strategy for triggering concerted ion transport [25], which proved effective for improving ionic conductivity in $LiTaSiO_5$ [25,33], $LiAlSiO_4$ [25], and $NaZr_2(PO_4)_3$ [34]. If more compositions capable of accepting extra Li^+ as interstitials can be identified, it is possible that strategic doping could be deployed to trigger concerted ion transport in a broader range of compounds/chemical systems.

In summary, the present work is predicated on two key assumptions. First, the "proximal stoichiometry" feature could be useful as a proxy for identifying disorder-tolerant or defect-rich compositions with low Li^+ vacancy/interstitial formation energies. Second, if extra Li^+ can be inserted into the structure owing to the tendency to preferentially form interstitial Li^+ defects upon doping, concerted ion transport may potentially be triggered. Regardless of transport mechanism, defect formation is always an essential aspect for ionic conduction, making it the primary focus of this work.

As a result, we designed inexpensive descriptors based on the aforementioned assumptions, along with other physical properties filters to down-select Li-containing compounds in the Materials Project (MP) database [35] in a high-throughput fashion. After the inexpensive screening process, two selected compositions (Li_7BiO_6, $Li_2B_4O_7$) were chosen for experimental synthesis/electrical measurements along with costly computational phase stability and defect calculations, to evaluate the efficacy of the descriptors and the implications of the "proximal stoichiometry" feature.

2. Methods

2.1. Inexpensive screening for new solid Li $^+$ conductors

2.1.1. "Proximal stoichiometry" descriptors

As described in Sec. 1, this effort aimed to design innovative descriptor sets capable of identifying new Li-disorder-tolerant compositions as candidates for solid electrolytes in ASSBs. To achieve this aim, we hypothesized that a "proximal stoichiometry" feature (compounds having nearby stable phases with similar Li stoichiometry) is indicative of flexibility in Li^+ coordination environment. We further hypothesized

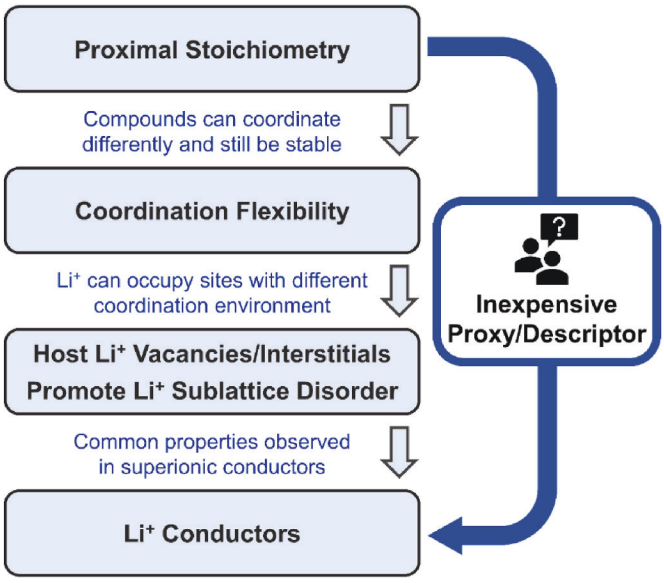

Fig. 1. Illustration of the main hypothesis of this work: "Proximal stoichiometry" is a feature that can be used as a computationally cheap proxy to search for new Li^+ conductors.

that such coordination flexibility can be associated with Li^+ sublattice/positional disorder and low Li^+ vacancy/interstitial formation energies. If Li^+ interstitials could be more readily inserted due to the ability to accommodate defects, concerted ion transport [24,25,33] may potentially be triggered.

A descriptor was designed to identify compounds exhibiting this "proximal stoichiometry" feature, and it was implemented in the following steps:

(1) Compounds with the same set of elements were categorized into their respective compositional space, with the atomic percentage of each element calculated.
(2) Compounds in each compositional space were arranged in the order of Li atomic percent. For each compound, the differences in Li atomic percent with its nearest neighbors were calculated.
(3) The difference in Li atomic percent must be smaller than set threshold for a given compound to pass through. In addition, when comparing two proximal compounds, the difference in ratios between non-Li elements must be smaller than 0.2. Considering $Li_2B_4O_7$ for example (B:O = 0.5714): the B:O ratios are 0.5 and 0.4286 for its nearest neighbors $LiBO_2$ and $Li_3B_7O_{12}$. As a result, both $LiBO_2$ and $Li_3B_7O_{12}$ were considered close to $Li_2B_4O_7$ since they satisfy both the Li-difference and non-Li-ratio criteria.

2.1.2. Additional physical descriptors

Additional filters were also applied, as the "proximal stoichiometry" descriptor alone does not include any information on electrical properties, structures, compound stability, etc. These properties could impact a compound's application as a solid electrolyte, and were therefore also obtained/calculated. Bandgap and energy above the convex hull were properties directly obtained from MP using pymatgen packages [35]: bandgap is related to intrinsic electronic conductivity; energy above the hull is associated with thermodynamic stability.

Bond valence migration energy ($E_{m,BV}$) [36,37] evaluates the electrostatic interactions between Li^+ and other immobile framework ions, and was used to ensure the framework scaffolds form conduction channels and allow for Li^+ conduction. Although there are some inherent limits in $E_{m,BV}$ calculations, it is one of the fastest routes to estimate Li^+ transport (1–2 min/structure on a personal computer); $E_{m,BV}$ had also been shown to be positively correlated with activation energies (E_A) calculated by DFT [38]. By first assigning the oxidation states of the ions with the program FormalCharges [12], bond valence migration energy ($E_{m,BV}$) could be calculated using the program BondStr [39].

Average Li–Li coordination number (CN_{Li-Li}) is a new descriptor implemented in this work, in order to evaluate the Li–Li interaction in a given compound. CN_{Li-Li} was calculated from the Li-sublattice in the following steps using pymatgen packages [35]:

(1) The Li-sublattice was obtained by removing all non-Li elements from the crystal structure.
(2) A 3 × 3 × 3 supercell was formed surrounding the original Li-sublattice.
(3) The distances between every Li in the center cell of the supercell and all the other Li in the supercell (d_{Li-Li}) were calculated.
(4) The shortest distance between Li ($d_{Li-Li,\ min}$) was determined for every Li in the center cell.
(5) For each Li in the center cell, if $d_{Li-Li} \leq 1.1 \times d_{Li-Li,min}$, the neighboring Li was considered to be coordinated. Rare instances where elongated 3 × 3 × 3 supercells were present (caused by primitive cells with very large/small angles) do not invalidate the calculations for Li–Li coordination number.
(6) After the Li–Li coordination number for each Li in the center cell was calculated, they were averaged to obtain CN_{Li-Li}.

With the aforementioned materials properties calculated, we begin to down-select compounds based on the materials properties in a high-throughput fashion using python scripts in a high-throughput fashion. The filtering steps/criteria will be discussed in greater depth in Sec. 3.1.1. Li_7BiO_6 and $Li_2B_4O_7$ were among the final candidates in the filtering process, and, for reasons expounded upon later in Sec. 3.1.2, were chosen for in-depth experimental/computational investigation in this work. Methods for experimental synthesis/characterization (Sec. 2.2, 2.3) and detailed computation calculations (Sec. 2.4) will be presented in the following sections.

2.2. Synthesis

2.2.1. $Li_{7+x}Bi_{1-x}Zr_xO_6$

Both undoped and Zr-doped Bi_2O_3 powders were synthesized using the citrate gel method [40,41]. Undoped Bi_2O_3 powders were synthesized by dissolving $Bi(NO_3)_3{\cdot}xH_2O$ in ethylene glycol, followed by the addition of citric acid. Zr-doped Bi_2O_3 powders ($Bi_{1-x}Zr_xO_{1.5+x/2}$, x = 0.05, 0.075, 0.1, 0.125, 0.2) were synthesized by first dissolving stoichiometric amounts of $ZrO(NO_3)_2{\cdot}xH_2O$ in deionized water, followed by the addition of citric acid. After stirring for 30 min at 80 °C, $Bi(NO_3)_3{\cdot}xH_2O$ was added, followed by balancing the pH to pH = 7 with addition of NH_4OH. The molar ratio of metal cations: citric acid was 1:6 for all samples. In both cases, the solution was stirred until a gel formed. The gel was then dried at 200 °C for 5 h and crushed. The dried gel was then calcined at 750 °C in air for 3 h and quenched in dry air to form Bi_2O_3/Zr-doped Bi_2O_3 powders. The Bi_2O_3/Zr-doped Bi_2O_3 powders were then mixed stoichiometrically with Li_2O (with 5% excess in Li to compensate for Li loss) in a mortar and pestle. The mixed powders were then pressed uniaxially under 125 MPa with a hydraulic press (Carver, Model 4350), followed by sintering in air to form $Li_{7+x}Bi_{1-x}Zr_xO_6$ pellets. Chemicals used include Li_2O (lithium (I) oxide, Thermo Scientific, 99.5%), $Bi(NO_3)_3{\cdot}5H_2O$ (bismuth(III) nitrate pentahydrate, Sigma-Aldrich, 99.99%), $ZrO(NO_3)_2{\cdot}xH_2O$ (zirconium(IV) oxynitrate hydrate, Sigma-Aldrich, 99%), $C_6H_8O_7$ (citric acid anhydrous, Thermo Scientific, 99.5%), $(CH_2OH)_2$ (ethylene glycol, Thermo Scientific). Water contents of starting reagents were measured by separate mass-loss analysis, in which the nitrates were decomposed into anhydrous oxides at high temperatures.

2.2.2. $Li_2B_4O_7$

$Li_2B_4O_7$ was synthesized using precipitation-assisted, solid-state synthesis, by dissolving stoichiometric amounts of Li_2CO_3 and H_3BO_3 in deionized water and heating gently until a viscous gel formed. Excess H_3BO_3 was added to compensate for B loss; details regarding the exact amount of excess B added will be discussed in later sections. The gel was then calcined at 650 °C for 1 h to form $Li_2B_4O_7$ powders; the calcination temperature was determined using thermogravimetric analysis (Fig. S12). Chemicals used include Li_2CO_3 (lithium carbonate, Thermo Scientific, 99.998%) and H_3BO_3 (boric acid, Thermo Scientific, 99.99%).

2.3. Characterization

Sample densities were determined from measured masses and geometries of the pellets, and expressed in terms of their respective theoretical densities (measured density/theoretical density = %TD). The phase content of the $Li_{7+x}Bi_{1-x}Zr_xO_6$ and $Li_2B_4O_7$ pellets was examined by X-ray diffraction (XRD) (Bruker D8 Advance XRD, Cu Kα-radiation, step size: 0.01°, time per step: 0.1 s, Panoramic Soller Slit). Rietveld refinements to all XRD data were performed using TOPAS with Powder Diffraction Files (PDF) from the International Centre for Diffraction Data (ICDD) database [42] for phase quantification and lattice parameter refinement.

The microstructure and grain size of the pellets were characterized by scanning electron microscopy (SEM) (JEOL 7000F Analytical SEM) and transmission electron microscopy (TEM) (JEOL 2010 LaB_6 TEM). Thermogravimetric analysis (TGA) was performed using a TA

Instruments Q50 Thermogravimetric Analyzer. For electrical measurements, electrodes were deposited by sputtering Au on both faces of the samples, and Pt wires were attached as current collectors. Two-point AC impedance spectroscopy measurements (Ametek/Solartron ModulabXM ECS impedance analyzer with femtoammeter and potentiostat attachments) were carried out in pure O_2 (UHP grade, flow rate of ~50 sccm) at various temperatures. All ionic conductivity measurements were carried out over a frequency range of 1 MHz–100 mHz. The impedance spectra were analyzed by equivalent circuit fitting in the frequency range of the sample responses (omitting electrode response), where Boukamp notation (R: resistance, Q: constant phase element) was used to describe the circuits. Selected impedance spectra were also analyzed with a "Distribution of Relaxation Times" (DRT) approach, using DRTtools software [43].

Geometric corrections according to the dimensions of the pellets were applied to calculate measured conductivities from the measured resistances. Assuming pores to be completely insulating, Bruggeman symmetric medium theory (Eq. (1)) was used to porosity-correct the conductivity for $Li_{7+x}Bi_{1-x}Zr_xO_6$ samples (≤90 %TD); asymmetric medium theory (Eq. (2)) was used for $Li_2B_4O_7$ samples (≥90 %TD) [44–46]. σ_m is the measured conductivity, σ_h is the porosity-corrected conductivity, representing the conductivity of the material matrix, and f is the volume fraction of the porosity. DC polarization experiments were performed using sputtered Au electrodes and a constant applied voltage of 0.1 V, with monitoring of the current as a function of time.

$$\sigma_h = \sigma_m \left(1 - \frac{3}{2}f\right)^{-1} \quad \text{Eq. (1)}$$

$$\sigma_h = \sigma_m (1-f)^{\frac{-3}{2}} \quad \text{Eq. (2)}$$

2.4. Detailed computational study

2.4.1. Structure relaxation and phase stability

The first-principles calculations were performed using the plane-wave basis Vienna *ab initio* simulation (VASP) package [47], implementing the Perdew-Burke-Ernzerhof generalized gradient approximation (PBE-GGA) functional [48]. We adopted the projector-augmented wave (PAW) [49] pseudopotentials to represent core electrons, with cores of [H] for Li, [Xe] for Bi, and [He] for B and O. A plane-wave energy cutoff of 340 eV and an automatically generated Γ−centered regular k-point mesh was used to sample the Brillouin zone for the primitive cells. During structural relaxation, the convergence criteria for energy and forces relaxations were set as 10^{-5} eV and 10^{-4} eV/Å respectively.

The thermodynamic stability of $Li_2B_4O_7$ and Li_7BiO_6 against decomposition into competing phases was determined using convex hull analysis. The competing phases (binary, ternary) considered in constructing the convex hull were obtained from the Inorganic Crystal Structure Database (ICSD) [50]. The total energies of the competing phases were calculated by geometry relaxation, using the same methodology as described above. The reference elemental chemical potentials of Li, Bi and B were calculated from their total energy. The chemical potential of O is sensitive to synthesis conditions and can be controlled by varying temperature or pressure. Therefore, we used realistic conditions for the chemical potentials of O at the assumed quenched-in temperature and pressure as obtained from thermodynamic tables [51]. The stability regions of $Li_2B_4O_7$ and Li_7BiO_6 in ternary chemical potential space are thermodynamically limited to several three-phase corners: at each corner the main phase is in equilibrium with 2 other competing phases. A python toolkit for visualizing phase stability and defect chemistry, VTAnDeM (github.com/ertekin-research-group/VTAnDeM), was utilized in this work for creating chemical potential phase diagrams.

2.4.2. Native defect energetics

To understand the defect chemistry, we employed the standard supercell approach [52] to calculate defect formation energies of native point defects. The defect formation energy ($\Delta E_{D,q}$) for a defect D in charge state q was calculated from density-functional theory (DFT) total energies according to the formula:

$$\Delta E_{D,q} = E_{D,q} - E_{host} + \sum_i n_i \mu_i + qE_F + E_{corr} \quad \text{Eq. (3)}$$

where $E_{D,q}$ and E_{host} are the total energies of the defective supercell and host supercell, respectively, E_F is the Fermi energy (electron chemical potential) relative to the valence band maximum (VBM), and E_{corr} is the correction term to the defect formation energies that accounts for the finite-size corrections within the supercell approach. The chemical potential of elemental species i is denoted by μ_i, n_i is the number of atoms of species i added ($n_i < 0$) or removed ($n_i > 0$) from the host supercell to form defects. μ_i is expressed as $\mu_i = \mu_i^0 + \Delta\mu_i$, where μ_i^0 is the reference elemental chemical potential (see section above) and $\Delta\mu_i$ the deviation from the reference chemical potential. The bounds on $\Delta\mu_i$ are determined by the thermodynamic stability condition, with $\Delta\mu_i = 0$ denoting i-rich conditions and negative values of $\Delta\mu_i$ corresponding to i-poor conditions.

Corrections to the defect formation energies E_{corr} arising from finite-size corrections were calculated using the approach proposed by Lany and Zunger[5]. Corrections implemented in this work include (1) image charge correction to account for long-range electrostatic interactions between charged defects and their periodic images across periodic boundaries, (2) potential alignment correction for charged defects to address misalignment of spatially average electrostatic potentials, and (3) band-filling corrections for shallow defects with Moss-Burnstein type band filling. The static dielectric constant (electronic + ionic contributions) needed for image charge correction was calculated using density functional perturbation theory (DFPT) [53].

The defect calculations were performed on a $Li_2B_4O_7$ primitive cell with 104 atoms and 2 × 2 × 2 supercell of Li_7BiO_6 with 112 atoms. The total energies were calculated by fully relaxing the atomic positions with fixed cell volume and cell shape for the optimized values for stoichiometric compound. A plane-wave energy cutoff of 340 eV and Brillouin zone sampling using a Γ-only k-point grid was used to relax the supercells. The native point defects considered in this work include vacancies (v_{Li}, v_B, v_{Bi}, v_O), anti-site defects (Li_O, O_{Li}, B_{Li}, Li_B, Bi_{Li}, Li_{Bi}, Bi_O, O_{Bi}, B_O, O_B) and interstitials (Li_i). The interstitials for Bi and O were not considered due to their relativey large ionic size. All native point defects are calculated in charged states ranging from −3 to +3. Moreover, all unique Wyckoff positions in the structure (see Fig. S17) were considered for vacancies, anti-site defects. The possible interstitial sites were determined using a Voronoi tessellation scheme. The pylada-defects software [54] was utilized in this work to automate point defect calculations for finding interstitial sites and calculation of finite-size corrections.

2.4.3. Defect and carrier concentrations

At thermodynamic equilibrium, the concentration of a defect $C_{D,q}$ can be obtained by:

$$C_{D,q} = Nexp\left(\frac{-\Delta E_{D,q}}{k_B T}\right) \quad \text{Eq. (4)}$$

where N is the density of the corresponding lattice sites to form the defects, k_B is the Boltzmann constant, T is the temperature, and $\Delta E_{D,q}$ is the formation energy of defects (see Sec. 2.4.2). To calculate the defect concentrations at thermodynamic equilibrium, the self-consistent solution for the Fermi energy for all native defects under the charge-neutrality condition must be obtained. The charge neutrality condition is given as:

$$\sum_D qC_{D,q} - n + p = 0 \quad \text{Eq. (5)}$$

where q is the charge state of the defects, and n and p are the free electron and hole concentrations, respectively. The charge-neutrality condition is valid at thermodynamic equilibrium and in the dilute regime where the defect concentration is sufficiently low such that defect-defect interactions are negligible.

When solving the charge-neutrality condition, we assume that most defect populations are "frozen-in" at synthesis temperatures when the system is cooled down to measurement temperatures due to the large kinetic barriers for the defects to re-equilibrate with the system at low temperatures. Since Li ions are mobile and can equilibrate with charge carriers at low temperatures, the defect concentrations for Li-related defects are calculated at measurement temperature.

3. Results

3.1. Descriptors

3.1.1. Implementing preliminary descriptors

In order to identify potential Li^+ conductors, the descriptors discussed in section 2.1 were used in series to down-select compounds from Materials Project. Among the descriptors used in this study, large band gap, low bond valence migration energy ($E_{m,BV}$), and low energy above the hull are properties generally considered beneficial for solid electrolyte applications; on the other hand, the "proximal stoichiometry" feature and average Li–Li coordination number (CN_{Li-Li}) are novel descriptors developed in this work. The filtering steps are illustrated in Fig. 2 and outlined here:

1. All Li-containing compounds were taken from MP and categorized into ternary, quaternary, or quinary compounds (binary compounds and others were excluded). At the time of search, there were 4840 ternary, 10507 quaternary, and 2401 quinary Li-containing compounds.
2. Ideally, a large bandgap is preferable for solid electrolyte materials to limit intrinsic electronic conductivity. Since bandgaps available from MP are calculated by DFT using the generalized gradient approximation (GGA) functional, they are often underestimated. Therefore, a relatively low cutoff value of >1 eV was chosen as a starting point.
3. Then, the "proximal stoichiometry" descriptor was implemented to find compounds with the "proximal stoichiometry" characteristic. Only compounds with at least one nearby compound within 10% Li atomic percentage (at%) difference in stoichiometry were chosen; this feature is denoted by "Li difference <10 at%" in Fig. 2.
4. Only compounds with a $E_{m,BV} < 1$ eV were chosen to rule out compounds with an unsuitable framework-ion sublattice for Li^+ transport. $E_{m,BV}$ tends to overestimate the actual activation energy, with a scaling factor of 0.3–0.7 compared to E_A calculated by DFT [12,38]. Since many superionic conductors have an E_A in the range of 0.2–0.5 eV [1,24,25], we believe an intermediate $E_{m,BV} < 1$ eV correlating to an E_A below 0.3–0.7 eV is a reasonable criterion.
5. $CN_{Li-Li} \geq 2$ was used as an indicator for potentially significant Li–Li interaction. For a given Li^+ ion, there will be many other nearby Li^+ ions interacting electrostatically. In addition, we hypothesized that a high CN_{Li-Li} may lead to the formation of a chain of closely situated Li^+ in the conduction channel, potentially migrating in a correlated fashion [25,34].
6. Only compounds with energy above hull ≤ 50 meV/atom were allowed to pass, ensuring their thermodynamic stability. Because of prediction errors of DFT calculations using the GGA functional [55], 50 meV/atom is used as a rule of thumb for phase stability.
7. Compounds containing potentially multivalent transition metals (V, Cr, Mn, Fe, Co, Ni, Cu) were excluded, to limit the probability of electronic conductivity.

There were also additional properties that were obtained/calculated, but not implemented as filters. For example, for a given compound, numbers of nearby phases within 5 at% Li stoichiometry difference were calculated. For another instance, information such as Li–Li distances, the coordination environments of Li^+ (ex. Li-anion/Li-cation coordination number) and the space groups of Li^+ sublattices were obtained for the compounds. A full list of properties can be found in SI Sec. 1, and the compounds selected in each step are listed in the excel files in the SI, along with all the materials properties calculated (3_Ternary_compound_data.xlsx, 4_Quaternary_compound_data.xlsx, 5_Quinary_compound_data.xlsx).

3.1.2. Descriptor results

After step (3), compounds that have at least one nearby phase within 10 at% Li stoichiometry were selected. It was found that several base structures for SICs were indeed able to pass through, including $LiLaTi_2O_6$ (LLTO), Li_3PO_4 (LISICON), $LiM_2(PO_4)_3$ (NASICON), Li_3OCl (antiperovskites), Li_3PS_4 (thio-LISICON), and $LiBH_4$ (borohydrides). Although some SICs such as LLZO, Li_6PS_5X (X = Cl, Br, I), and $Li_{10}GeP_2S_{12}$ (LGPS) were filtered out at the time of descriptor implementation, it was later found that their omission was due to incompleteness of the database. Owing to a recent update, LLZO and Li_6PS_5Cl now indeed exhibit the "proximal stoichiometry" characteristic and pass through the filter step (3). For $Li_7La_3Zr_2O_{12}$ garnet, $Li_{4.75}La_3Zr_2O_{12}$ (mp-1239180) and $Li_{4.25}La_3Zr_2O_{12}$ (mp-1120817) were recently added as proximal phases; for Li_6PS_5Cl argyrodite, $Li_5PS_4Cl_2$ was added. From our initial screening, many SICs satisfied the "proximal stoichiometry" criterion, which motivated our exploration of other compounds sharing a similar characteristic as candidates for new Li^+ conductors.

While considerably narrowed down, 1244 ternary, 670 quaternary, and 100 quinary compounds after step (3) were still too many compositions for computationally costly calculations or experimental work. Therefore, candidates for experimental testing and in-depth computation were chosen after step (7), where the number of remaining compounds was reasonable for human analysis. These compounds, listed in the excel sheets in SI, additionally exhibited low $E_{m,BV}$ and high CN_{Li-Li}, which were considered to be desirable properties for Li^+ transport in this work. Low energy above the convex hull and the exclusion of transition

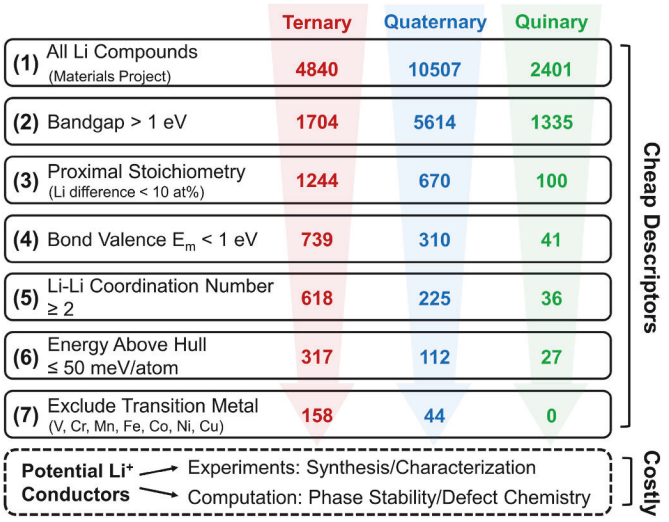

Fig. 2. Workflow of the filtering process: the "proximal stoichiometry" descriptor along with additional physical properties filter were implemented to down-select compounds from Materials Project [35]. Step (1)–(7) were cheap descriptions that can be implemented in a high-throughput fashion. Afterwards, candidates can be chosen for costly calculations and experiments.

metal ions were also advantageous for compound stability and application as a solid electrolyte. Among the compounds after step (7), Li_7BiO_6 and $Li_2B_4O_7$ were selected as candidates for costly experimental/computational investigation in this work, with their properties listed in Table 1. Li_7BiO_6 and $Li_2B_4O_7$ exhibited an even stronger "proximal stoichiometry" characteristic than the criteria set in step (3) (at least one nearby phase within 10 at% Li stoichiometry difference), with two nearby phases within 5 at% Li stoichiometry difference. We hypothesized that this attribute may correlate strongly with coordination flexibility and potentially high ionic conductivity. While there were still over 50 compounds exhibiting this attribute, Li_7BiO_6 and $Li_2B_4O_7$ were relatively unexplored oxide compositions (from the perspective of electrolytes), with reasonably simple chemistries (low number of cations) and potential air-stability as oxides, which may be less challenging than some others in terms of synthesis. Therefore, they were explored first; other compounds could be of interest in future work.

Li_7BiO_6 was pursued initially, given its high Li^+ concentration, which could lead to a high conductivity pre-factor. It also has 3D conduction channels with relatively low $E_{m,BV}$ that are beneficial for ion movements. Lastly, Li_7BiO_6 includes both tetrahedral and octahedral sites in the structure [56], which could satisfy the high-energy/low-energy sites configuration theorized to be ideal for concerted ion transport [25]. Although some studies have previously characterized the ionic conductivity of Li_7BiO_6 [56–60], no systematic manipulation of $Li_i^{\bullet}$ or v_{Li}' through doping has been reported. Therefore, in this work, we explored the defect chemistry and attempted to introduce $Li_i^{\bullet}$ through aliovalent doping in Li_7BiO_6. In addition, only total conductivities have been reported for Li_7BiO_6 [56–60], whereas systematic separation of microstructural contributions to overall transport processes (bulk/grain vs. grain boundary transport etc.) has not been tackled prior to this work, leaving open questions regarding the magnitude of the true bulk conductivity.

$Li_2B_4O_7$ was pursued secondarily, despite having a lower Li concentration, as it also exhibited a low $E_{m,BV}$, with a reported experimental E_A of 0.46 eV for Li^+ transport measured in a single crystal [61]. It was additionally predicted to have a 1-D conduction channel with low E_A of 0.27–0.37 eV using DFT [62]. In terms of doping studies, most research focused on its application towards thermoluminescent dosimetry applications [63–66], whereas doping studies intended for introducing $Li_i^{\bullet}$ or v_{Li}' to modify ionic conductivity were limited. This knowledge gap motivates the exploration of the relationship between defect chemistries and ionic conductivity in $Li_2B_4O_7$ in this work.

3.2. Experimental testing on new compositions

In this section, we describe the effectiveness of the descriptors according to experimental characterization of the two filtered compositions in Table 1, Li_7BiO_6 and $Li_2B_4O_7$. In-depth phase analysis and electrical measurements were carried out for both systems, to evaluate the feasibility of excess Li^+ insertion and potential activation of the concerted ion transport mechanism.

Table 1
Two of the practical compositions of interest in this work for synthesis/characterization and in-depth computation based on the descriptors. Li_7BiO_6 and $Li_2B_4O_7$ exhibited an even stronger "proximal stoichiometry" characteristic than the criterion set in step (3) in Fig. 2, which we hypothesized may correlate strongly with coordination flexibility and potentially high ionic conductivity. An experimental band gap of 2.85 eV was reported for Li_7BiO_6 [67], larger than the theoretical band gap calculated in MP (calculations by DFT using the generalized gradient approximation functional are known to underestimate band gaps). There are over 50 other compounds with similar features listed in the Excel sheets in SI that can be of interest for future work.

Composition	MP Bandgap (eV)	$E_{m,BV}$ (eV)	Number of Proximal Compositions (within 5 at% Li difference)	CN_{Li-Li}
Li_7BiO_6	1.861	0.68	2	3.29
$Li_2B_4O_7$	5.668	0.69	2	2.00

3.2.1. Li_7BiO_6: phase stability and electrical properties

Li_7BiO_6 includes both tetrahedral and octahedral sites in the structure [56], with the tetrahedral sites fully occupied and the octahedral sites partially occupied [35,58]. If excess Li^+ could be added to the already high Li^+ concentration through aliovalent doping, concerted ion transport could potentially be triggered, by shifting the distribution of Li^+ among sites with different energies and increasing Li–Li interactions. To introduce acceptors that could be compensated by $Li_i^{\bullet}$, Zr^{4+} (0.72 Å) was doped on the Bi^{+5} (0.76 Å) site, making the final composition $Li_{7+x}Bi_{1-x}Zr_xO_6$ (x = 0, 0.05, 0.075, 0.1, 0.125, 0.2).

As seen in Fig. 3, XRD patterns of the $Li_{7+x}Bi_{1-x}Zr_xO_6$ samples showed no impurity phase when $x \leq 0.1$, while the presence of ZrO_2 and Li_2CO_3 was detected in x = 0.125 and 0.2. This finding likely indicated that the solubility limit of Zr^{4+} in the Li_7BiO_6 phase was around 10%, and excess Li^+ and/or Zr^{4+} led to the formation of impurity phase(s). Close examination showed that peak intensities also varied as the amount of Zr^{4+} increased, suggesting Zr^{4+} ions were able to substitute for Bi^{5+} in Li_7BiO_6 (Fig. S1). On the other hand, the peak positions were invariant as the amounts of dopants increased, which may be due to $Li_i^{\bullet}$ countering any lattice contraction from the slightly smaller Zr^{+4} ions. The XRD patterns for samples annealed in O_2 at 400 °C for 8 h remained similar to as-sintered samples (Fig. S3), while the microstructure changed from a mix of crystalline and amorphous-like phase (obtained immediately after sintering) to a crystalline-dominant structure after O_2-annealing (Fig. 4). Relative densities of all $Li_{7+x}Bi_{1-x}Zr_xO_6$ samples were in the range of 70–80%; detailed information on the densities and phase fractions can be found in Table S1.

In terms of electrical properties, DC polarization experiments

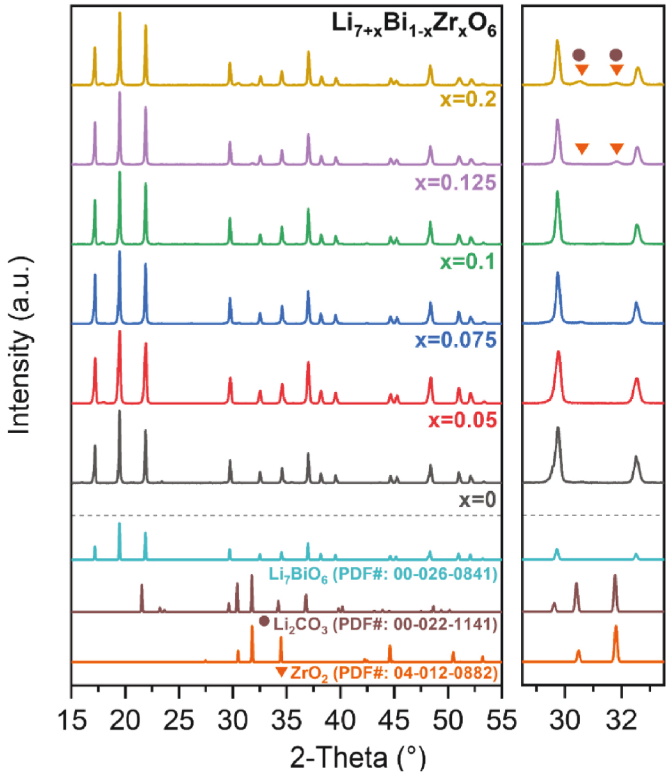

Fig. 3. XRD patterns of $Li_{7+x}Bi_{1-x}Zr_xO_6$ (x = 0, 0.05, 0.075, 0.1, 0.125, 0.2) were plotted above the broken line; reference patterns for phase analysis were shown below the broken line. Impurity phases like ZrO_2 and Li_2CO_3 were observed for x = 0.125 and 0.2, suggesting the solubility limit of Zr in Li_7BiO_6 was around 10%.

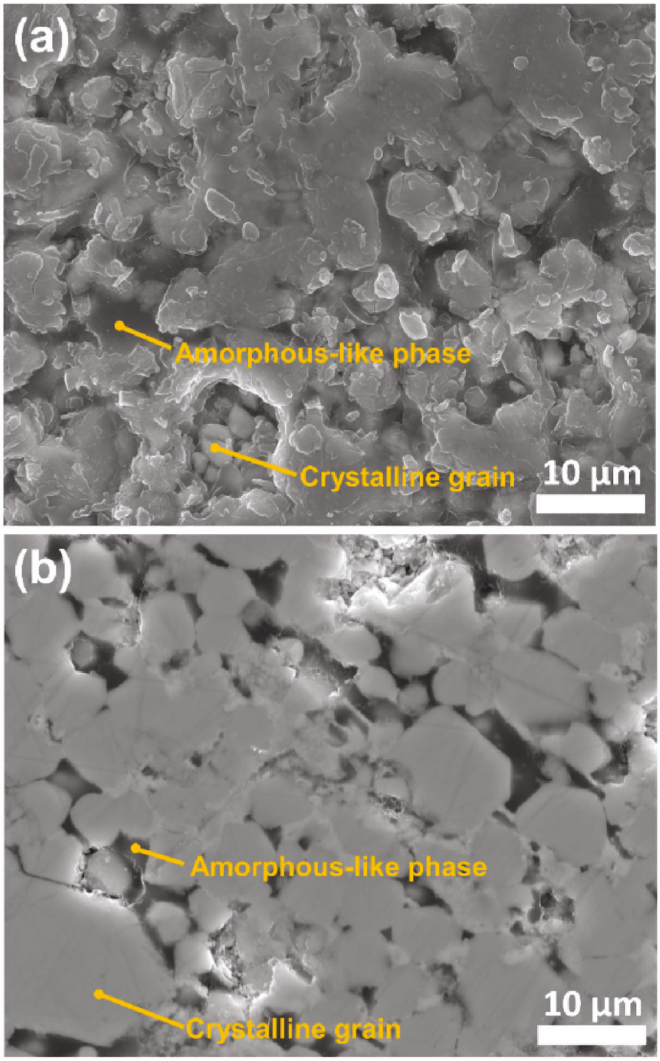

Fig. 4. SEM images of (a) as-sintered $Li_{7.05}Bi_{0.95}Zr_{0.05}O_6$ and (b) 400 °C 8 h O_2-annealed $Li_{7.05}Bi_{0.95}Zr_{0.05}O_6$. Before annealing, both crystalline grains and amorphous-like phase could be observed; after annealing, crystalline grains became more dominant, and the amorphous-like phase volume was reduced significantly. Similar microstructures were found for other $Li_{7+x}Bi_{1-x}Zr_xO_6$ samples.

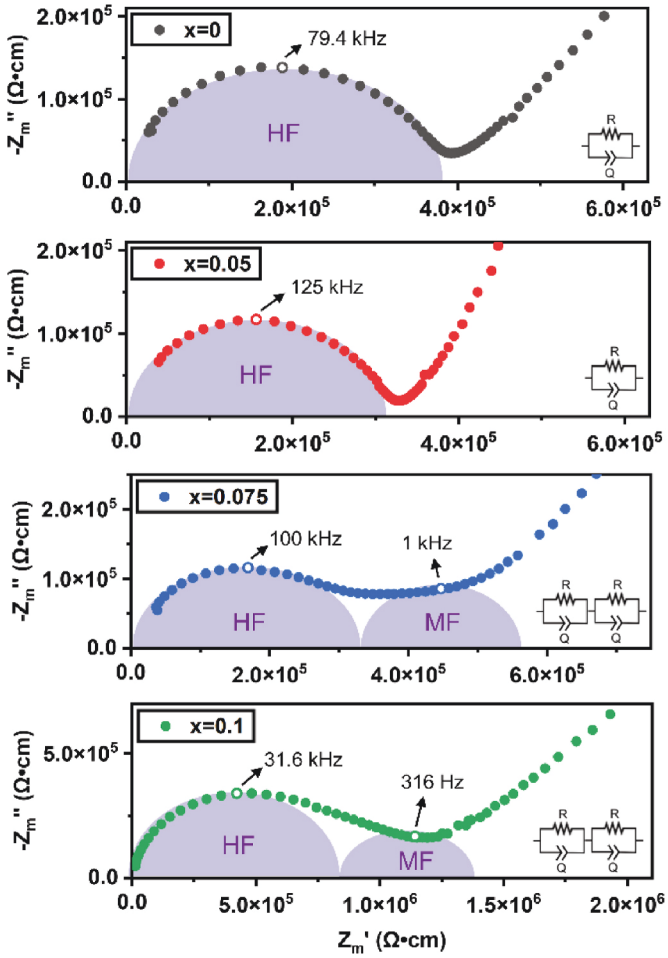

Fig. 5. Nyquist plots of 400 °C O_2-annealed $Li_{7+x}Bi_{1-x}Zr_xO_6$ as a function of dopant concentration at 28 °C: High frequency (HF) arcs were attributed to bulk transport, whereas middle frequency (MF) arcs were attributed to grain boundaries or residual amorphous phase transport. The hollow data points mark the tops of the HF and MF arcs. For x = 0 and x = 0.05, MF arcs were absent above 28 °C; they were only observed below 28 °C. More discussion can be found in SI Sec. 2.5. (Z_m' and Z_m'' were respectively the real and imaginary part of the impedance that were geometry-corrected and not porosity-corrected. The equivalent circuits used to analyze the spectra were drawn on the bottom-right corners of each spectrum. The semicircles served as approximate eye guides for how the impedance responses were fitted.)

showed that the measured current decayed rapidly with respect to time under constant voltage, confirming that $Li_{7+x}Bi_{1-x}Zr_xO_6$ compositions were primarily Li^+ conductors with low electronic and oxide-ion transference numbers (Fig. S2). Impedance spectroscopy measurements were performed for both as-sintered and 400 °C 8 h O_2-annealed samples, with their Nyquist plots shown in Fig. 5 and SI Sec. 2.5. The annealing step was taken to ensure dehydration of the samples and consequently minimize the effect of protons on conductivity; it also led to a change in impedance response in the Nyquist plots (SI Sec. 2.5), resulting in higher total conductivities compared to unannealed (as-sintered) samples. Corresponding to the microstructure evolution (Fig. 4), the change in impedance spectra was likely due to the elimination of the residual amorphous phase in as-sintered samples. More discussion of the effect of annealing and the interpretation of Nyquist plots is presented in SI Sec. 2.5, while the bulk (grain) conductivities of annealed samples are the focus in the main text.

Typical Nyquist plots of $Li_{7+x}Bi_{1-x}Zr_xO_6$ after annealing in O_2 at 400 °C for 8 h were shown in Fig. 5. From the analysis in SI Sec. 2.5, the high frequency (HF) arcs were attributed to bulk transport in the crystalline grains, whereas the middle frequency (MF) arcs could be caused by grain boundaries or residual amorphous phase. Fig. 6 showed the bulk conductivity of annealed $Li_{7+x}Bi_{1-x}Zr_xO_6$. The extrapolated porosity-corrected bulk conductivity ($\sigma_{h,bulk}$) at 30 °C was 4.15×10^{-6} S/cm. At x = 0.05, when 5% of Zr^{4+} and extra Li^+ were introduced, the conductivity increased by just over 50% to $\sigma_{h,bulk,30°C} = 6.45 \times 10^{-6}$ S/cm. However, higher dopant concentrations (x ≥ 0.075) did not follow the same increasing trend in conductivity; instead, the conductivities for x = 0.075 were lower than for x = 0.05 and continued to decrease from x = 0.075 to x = 0.1. The conductivities for x = 0.1 and x = 0.125 were nearly identical, suggesting that the solubility limit was likely reached—consistent with the XRD results. Moreover, the activation energies remained nearly unchanged as a function of dopant concentration. These results suggested that while Li_7BiO_6 was dopable and $Li_i^{\bullet}$ helped improve conductivity to some degree, the benefits were limited. The fact that E_A remained independent of dopant concentration also suggested that doping did not trigger concerted ion transport behavior in $Li_{7+x}Bi_{1-x}Zr_xO_6$.

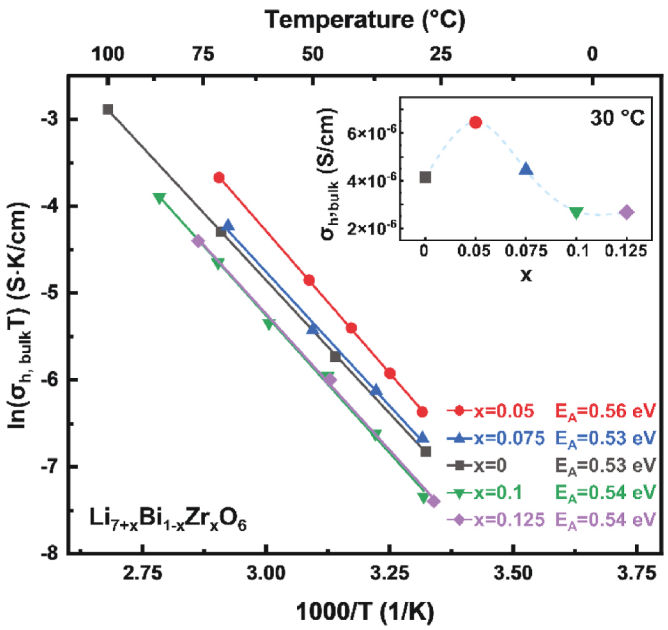

Fig. 6. Porosity-corrected bulk conductivities ($\sigma_{h,bulk}$) of $Li_{7+x}Bi_{1-x}Zr_xO_6$ as a function of dopant concentration (x) and temperature. The inset showed the $\sigma_{h,bulk}$ at 30 °C for different Zr concentrations. Compared to x = 0, the bulk conductivity increased for x = 0.05. Higher dopant concentrations then led to a reversal of the trend, whereas bulk conductivity remained the same for x ≥ 0.1. The activation energies were nearly invariant with respect to Zr content.

3.2.2. $Li_2B_4O_7$: phase stability and electrical properties

Precipitation-assisted solid-state synthesis [68] was used to synthesize $Li_2B_4O_7$ powders and pellets. The following processing challenges made it difficult to obtain phase pure and dense $Li_2B_4O_7$ samples: (1) B evaporates during sintering; (2) densification behavior changes drastically with small variations in Li:B ratio and sintering temperature. Clearly these factors were closely coupled, making the actual Li:B ratio in the sample difficult to control, and $LiBO_2$ and $Li_3B_7O_{12}$ impurity phases formed easily in all samples. The presence of either Li-rich or Li-poor secondary phases, depending on overall stoichiometry, also suggested that the $Li_2B_4O_7$ phase did not accommodate much flexibility in Li stoichiometry. Because of the challenges mentioned above, instead of obtaining completely phase pure samples, small amounts of $LiBO_2$ or $Li_3B_7O_{12}$ were formed intentionally in the samples, by adding different amounts of extra B in the initial solution, with a combination of different processing techniques. In this case, for samples in thermodynamic equilibrium, the Li^+ concentration in the $Li_2B_4O_7$ phase could be assumed to be pinned at its upper limit when $LiBO_2$ was present (Li-rich samples) and pinned at its lower limit when $Li_3B_7O_{12}$ was present (Li-poor samples). With a combination of high-energy ball milling, spark plasma sintering (SPS), and conventional heat treatment, dense Li-rich and Li-poor $Li_2B_4O_7$ samples were obtained. The phase fractions/densities of the $Li_2B_4O_7$ samples are listed Table 2, with their XRD patterns plotted in Fig. S13.

Before analyzing the electrical properties of the Li-rich and Li-poor $Li_2B_4O_7$, we surveyed the literature for transport properties of the observed impurity phases $LiBO_2$ and $Li_3B_7O_{12}$. The ionic conductivity of $LiBO_2$ was reported to be ~4 times higher than those of $Li_2B_4O_7$ measured in this work [69], whereas the ionic conductivity of $Li_3B_7O_{12}$ was unexplored to our knowledge. Regardless, because of their small volume fractions (<5 vol%), $LiBO_2$ and $Li_3B_7O_{12}$ were assumed to have negligible effects on the electrical properties. The relative densities were also high, indicating only minor porosity corrections to the electrical data were needed.

$Li_2B_4O_7$ samples were confirmed to be primarily Li conductors using DC polarization experiments (Fig. S16), with a Li^+ transference number of 0.991—consistent with the large band gap shown in Table 1. For the Li^+ conductivity measurements, Li-rich and Li-poor $Li_2B_4O_7$ were held in dry O_2 at 300 °C for 8 h for possible dehydration before temperature-dependent impedance spectroscopy measurements, during which time no change in conductivity was observed. The Nyquist plots (Fig. 7) appeared to reveal two poorly resolved processes; these processes could be resolved more clearly in the DRT spectra (Fig. 7(c)(f)). For Li-rich $Li_2B_4O_7$, the relative permittivities (ε_r) were 69–74 for the HF process, with a HF capacitance of 3.7×10^{-11} - 4.0×10^{-11} F and a MF capacitance of $4.7 \times 10^{-11} - 5.3 \times 10^{-11}$ F; for Li-poor $Li_2B_4O_7$, ε_r were 65–69 for the HF process, with a HF capacitance of $1.1 \times 10^{-11} - 1.2 \times 10^{-11}$ F and a MF capacitance of $1.0 \times 10^{-11} - 1.2 \times 10^{-11}$ F. These HF ε_r values were comparable to those reported in other work on $Li_2B_4O_7$ [70]. Based on the crystalline microstructure (Fig. S14) and the assumption that grain boundaries were blocking, the HF and MF portions of the spectra were attributed respectively to bulk (grain) and grain boundary processes in the main phase, $Li_2B_4O_7$. Using the HF portion from the spectra (e.g., highlighted portion in Fig. 6), the bulk conductivities were determined and are plotted in Fig. 8. The $\sigma_{h,bulk}$ of the Li-rich sample was only slightly higher than that of the Li-poor sample, indicating that the intrinsic change in defect concentration may be limited between Li-rich and Li-poor conditions, and that the influence of secondary phases were negligible. The total conductivities (including both grain and grain boundary contributions) were also similar, as seen in Fig. S15. These electrical findings are consistent with the XRD results demonstrating a narrow width to the phase and indicating that variation in Li stoichiometry in the $Li_2B_4O_7$ phase is limited.

3.3. Computational phase stability/defect chemistry analysis of Li_7BiO_6 and $Li_2B_4O_7$

In addition to experimental testing, it was also important to determine computationally the phase stability and defect chemistries of Li_7BiO_6 and $Li_2B_4O_7$. Through computational convex hull construction (Sec. 2.4), it was determined that both $Li_2B_4O_7$ and Li_7BiO_6 are thermodynamically stable phases. To realize quantitative control of Li stoichiometry, it was important to understand the native defect chemistry of Li_7BiO_6 and $Li_2B_4O_7$. In this work, we employed a thermodynamic defect model that considers a broad range of native point defects (vacancies, anti-site defect, interstitials) in all possible charge states (see Sec. 2.4.2, Sec. 2.4.3), which had been shown to obtain more accurate equilibrium defect concentrations than simple vacancy-compensation model [71].

3.3.1. Computational thermodynamic phase analysis

The calculated Li–Bi–O ternary phase diagram was shown in both composition and chemical potential space (Fig. 9 (a)). In the chemical potential space of Li_7BiO_6, the stability region was limited by a range of Li, Bi, and O chemical potentials shown by the grey shaded region. We found that Li_7BiO_6 was stable over a limited range of Li chemical potentials, with $\Delta\mu_{Li}$ varying from −2.27 to −2.69 eV. The limited stability region was expected, given the proximal stoichiometry requirement that

Table 2
Phase fractions/densities of the Li-rich and Li-poor $Li_2B_4O_7$ samples for electrical measurements.

Sample	Extra B added	Synthesis Route	$Li_2B_4O_7$ (wt%)	$LiBO_2$ (wt%)	$Li_3B_7O_{12}$ (wt%)	Density (%TD)
Li-rich	1%	High Energy Ball Milling + Conventional Sintering 805 °C 12 h	98.6	1.4	0.0	99.0%
Li-poor	2.5%	SPS 750 °C 50 MPa 3min + Post Annealing 800 °C 9 h	96.3	0.0	3.7	91.6%

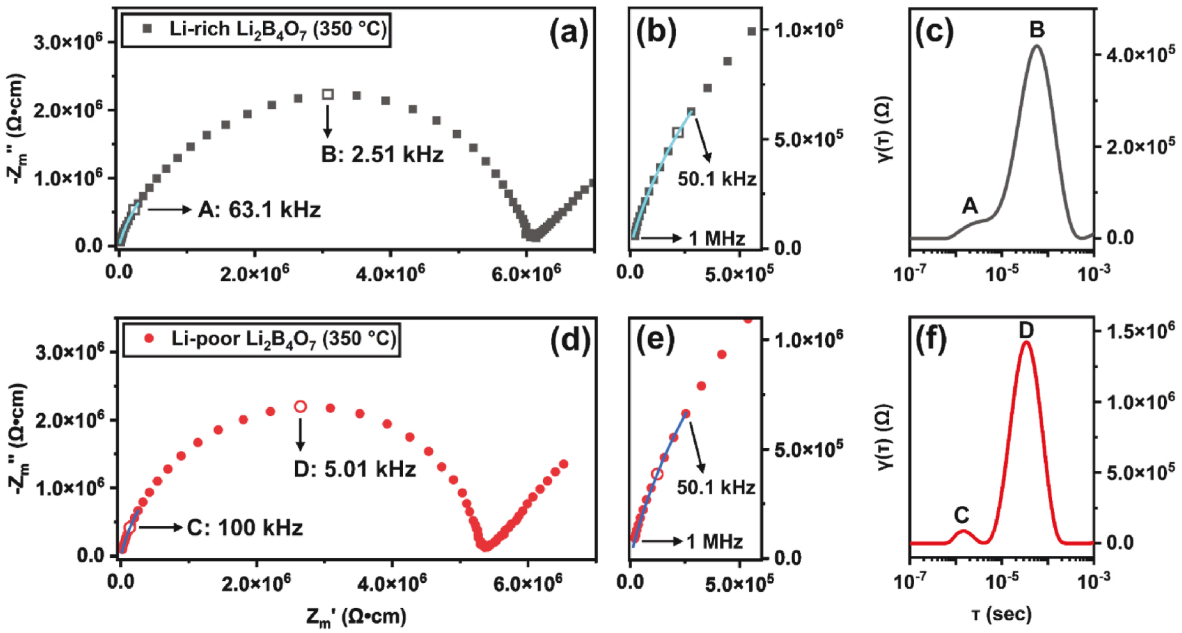

Fig. 7. (a)(d) Nyquist plots of Li-rich and Li-poor $Li_2B_4O_7$ measured at 350 °C. (b)(e) Zoomed-in view of the high-frequency portion of the Nyquist plots. (c)(f) DRT spectra in the frequency range of the sample responses (omitting electrode response), to help deconvolute Nyquist plots. The DRT analysis revealed 2 processes for both Li-rich and Li-poor $Li_2B_4O_7$; these peaks corresponded to the hollow data points on the Nyquist plots, with their respective frequencies listed. The bulk conductivities in Fig. 8 were fitted from the highlighted solid lines high-frequency (HF) portion of the arcs (1 MHz-50.1 kHz) using one (RQ) equivalent circuit.

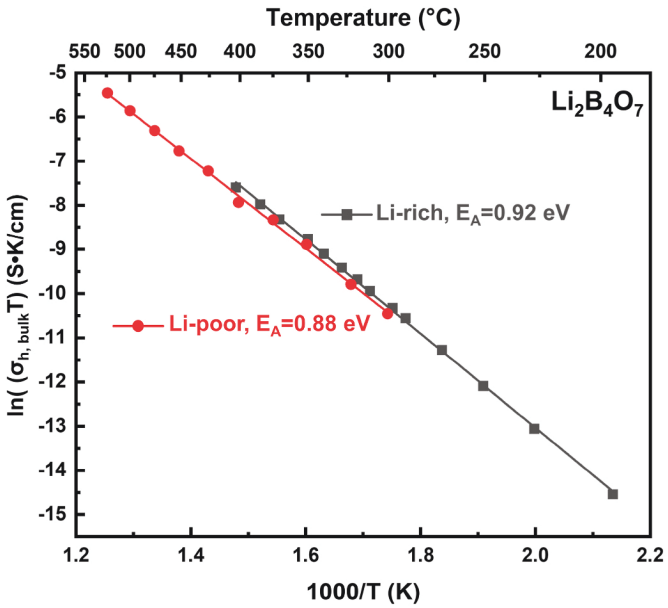

Fig. 8. Porosity-corrected bulk conductivities ($\sigma_{h,bulk}$) of the Li-rich and Li-poor $Li_2B_4O_7$ samples listed Table 2. The bulk conductivities were determined from fitting the high-frequency portion of the impedance spectra, e.g., as shown in Fig. 7. Li-rich samples were only slightly more conductive than the Li-poor samples, and the activation energies were similar.

introduced competing phases of similar stoichiometry. The limited tunability of $\Delta\mu_{Li}$ indicated that the defect formation energies and concentrations of Li interstitials and Li vacancies within the Li_7BiO_6 phase would not change much by regulating the stoichiometry/chemical potentials during experimental synthesis. We found that the phase stability region of Li_7BiO_6 was bounded by 4 three-phase corners where Li_7BiO_6 is in equilibrium with 2 other competing phases. At the most Li-rich synthesis condition (D), Li_7BiO_6 was in equilibrium with Li_2O (cubic, *Fm*-3*m*) and Li_3BiO_3 (triclinic, *P*1). At the most Li-poor synthesis condition (A), Li_7BiO_6 was in equilibrium with Li_5BiO_5 (monoclinic, *Cm*) and elemental O. Since Li_7BiO_6 was synthesized in ambient air, we concluded that the real synthesis condition should be located between corner A and B where Li_7BiO_6 was in equilibrium with elemental O under O-rich synthesis conditions ($\Delta\mu_O = 0.0$ eV).

The calculated Li–B–O ternary phase diagram and chemical potential space were shown in Fig. 9(b). Similarly, $Li_2B_4O_7$ was only thermodynamically stable over a narrow window (Fig. 9(b)). We found that the phase stability region of $Li_2B_4O_7$ was bounded by 4 three-phase corners. For all three-phase corners, $Li_2B_4O_7$ was in equilibrium with B_6O or elemental O, with $LiBO_2$ (monoclinic, $P2_1/c$) being the third phase in more Li-rich synthesis conditions (G, H) and $Li_3B_7O_{12}$ (triclinic, *P*-1) in more Li-poor conditions (E, F). In the chemical potential space, the stability region of $Li_2B_4O_7$ exhibited a "stick-like" shape, with small tunability window for $\Delta\mu_{Li}$ and large tunability window for $\Delta\mu_B$ (from −0.17 to −6.04 eV) and $\Delta\mu_O$ (from 0 to −3.92 eV). A small deviation of $\Delta\mu_{Li}$ would lead to the formation of impurity phase $LiBO_2$ or $Li_3B_7O_{12}$, as observed in our experiments (see Sec. 3.2.2). The narrow range of $\Delta\mu_{Li}$ would result in small variation of defect formation energies for Li vacancy and interstitial defects (see Eq. (3)) throughout the stability region. Again, since $Li_2B_4O_7$ was synthesized in ambient air and in equilibrium with elemental O, we can conclude that point E and F corresponded to synthesized Li-poor and Li-rich samples respectively by matching the impurity phases.

3.3.2. *Defect chemistries*

To explore the doping response of Li_7BiO_6, we performed defect analysis on Li_7BiO_6 at different chemical potential conditions that may be accessed synthetically. The range of chemical potentials under which Li_7BiO_6 was predicted to be thermodynamically stable lies between O-rich/Li-poor and O-poor/Li-rich limits (Fig. 9(a)). For both O-rich/Li-poor and O-poor/Li-rich synthesis conditions, the formation energies ($\Delta E_{D,q}$) of the native point defects in Li_7BiO_6 were shown in Fig. 10. The defect chemistry did not change much at different chemical potentials (hypothetical synthesis conditions) due to the lack of chemical potential tunability in the narrow stability region, and our discussion will focus on

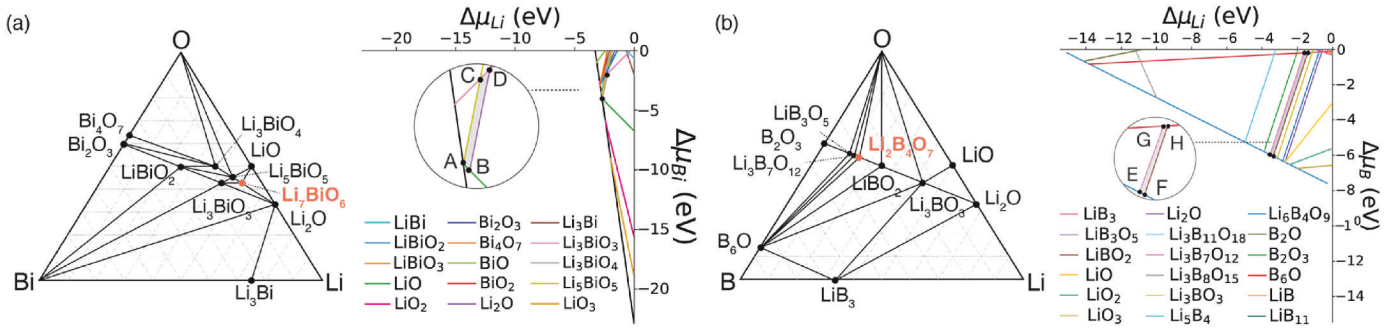

Fig. 9. The phase stability region of Li_7BiO_6 (a) and $Li_2B_4O_7$ (b) in the composition space (left) and chemical potential space (right). The stability region in chemical potential space was shown by the grey-shaded region. The circular insets showed the zoomed-in views on the stability windows.

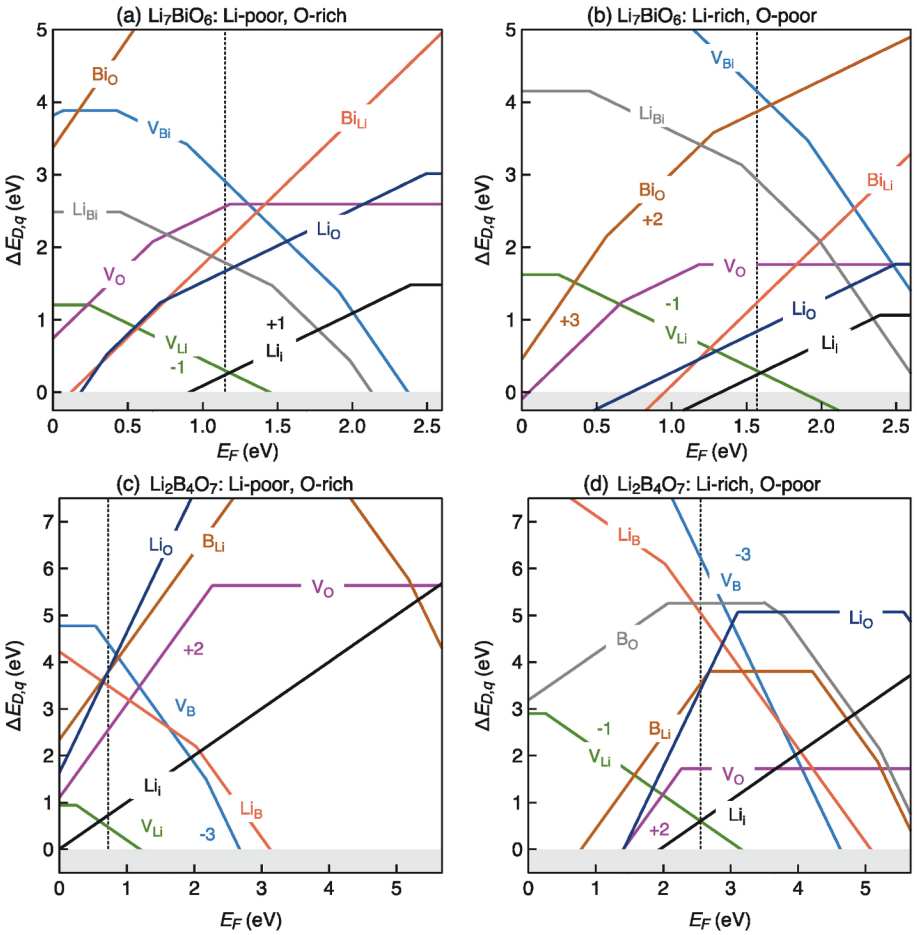

Fig. 10. Formation energies of native point defects ($\Delta E_{D,q}$) as a function of Fermi energy (E_F) in Li_7BiO_6 under the (a) Li-poor/O-rich and (b) Li-rich/O-poor synthesis conditions, and $Li_2B_4O_7$ under the (c) Li-poor/O-rich and (d) Li-rich/O-poor conditions. Li interstitials $Li_i^{\bullet}$ were placed in the tetrahedral interstitial site. The self-consistent Fermi energy was shown by the dashed vertical line calculated at synthesis temperature (873 K for Li_7BiO_6 and 673 K for $Li_2B_4O_7$). The calculated GGA band gaps for Li_7BiO_6 and $Li_2B_4O_7$ were 2.60 and 5.67 eV respectively. For the sake of clarity, only the lowest energy Wyckoff site for each defect was shown. See the defect diagrams with all defects in Figs. S18 and S19.

O-rich/Li-poor condition, which is close to our experimental condition carried out in ambient oxygen. We found that Li-related defects (v_{Li}', $Li_i^{\bullet}$) were the dominant defects in Li_7BiO_6 with the lowest formation energies. The lowest energy $Li_i^{\bullet}$ defect was located at the tetrahedral interstitial site (See Fig. S17). These two lowest energy defects compensated each other and thereby pinned the equilibrium Fermi energy (E_F^{eq}) around mid-gap. Using the "frozen defect" model (Sec 2.1.4), the estimated defect formation energies for v_{Li}' and $Li_i^{\bullet}$ were 0.30 eV and 0.24 eV, leading to defect concentrations of 3.1×10^{18} and 3.2×10^{18} cm^{-3}, respectively, at an operating temperature of 873 K. The results of the defect analysis were consistent with our premise that intrinsic Li^+ conductors may be identified from materials families that potentially support Li coordination flexibility, and that such compounds would exhibit disorder in the form of high concentrations of Li vacancies and interstitials.

Similarly, the dominant defects in $Li_2B_4O_7$ with the lowest formation energies were also Li-related (v_{Li}' and $Li_i^{\bullet}$). However, due to the high-aspect-ratio "stick-like" phase stability region of $Li_2B_4O_7$, the achievable chemical potentials of $Li_2B_4O_7$ spanned a range of values changing from the most Li-rich region (points G, H in Fig. 9) to the most Li-poor region (points E, F in Fig. 9), and the defect chemistries of $Li_2B_4O_7$ at Li-rich/O-poor and Li-poor/O-rich synthesis conditions were, therefore, very different as shown in Fig. 10. At a Li-rich/O-poor synthesis condition, the crossing point of v_{Li}' and $Li_i^{\bullet}$ was close to mid-gap; while at a Li-poor/O-rich synthesis condition, the equilibrium Fermi energy was pinned closer to the valence band maximum. For Li-poor conditions, which more closely represented experiment conditions, the predicted formation energies of v_{Li}' and $Li_i^{\bullet}$ were 0.48 and 0.72 eV, leading to

defect concentrations of 3.5 × 10^{18} and 4.7 × 10^{13} cm^{-3} 673 K, respectively; at Li-rich conditions, both defects had a defect formation energy of 0.6 eV and a predicted concentration of 4.0 × 10^{14} cm^{-3}.

4. Discussion

4.1. Effect of Li^+ insertion on Li_7BiO_6 and $Li_2B_4O_7$

4.1.1. Defect chemistries/electrical properties of $Li_{7+x}Bi_{1-x}Zr_xO_6$

With the presence of both tetrahedral and octahedral sites in Li_7BiO_6 [56], we hypothesized these sites may be different in energy for Li^+ to occupy, which could satisfy the high-energy/low-energy sites configuration theorized to be ideal for concerted ion transport [25]. The Li_7BiO_6 structure at 0 K from MP suggests that the tetrahedral sites were fully occupied and the octahedral sites were partially occupied [35,58], which was indicative that the tetrahedral sites were lower in energy. As a result, we hypothesized that the introduction of extra Li^+ would shift the distribution of Li^+ among sites of different energies, potentially triggering concerted ion transport.[56] In Sec. 3.2.1, XRD showed that aliovalent Zr^{4+} can be doped onto Bi^{5+} sites up to around 10%, while the impedance results suggested that the acceptor doping in the presence of compensating Li at least initially introduced the desired Li^+ interstitials into the lattice. Zr doping first led to an improvement in the bulk conductivity when $x = 0.05$, but additional Zr started to lower the bulk conductivity again, down to the apparent XRD solubility limit ($x \geq 0.1$), after which the conductivity remained unchanged with further Zr addition. This result indicated that the defect concentration/distribution did not continue to vary in the primary phase after the dopant solubility limit was reached. Concerning the conductivity decrease for $x > 0.05$, it is possible that there were too many Li^+ (less available vacant sites) in the conduction channel as $x > 0.05$, such that the ratio between concentrations of mobile ions and available sites became suboptimal. As can be seen in Eq. (S1), isolated hopping conductivity can be optimized when the product of carrier concentration and available sites is maximized [24].

Aside from the magnitude of the bulk conductivity, the activation energy E_A as a function of dopant content can be informative. The invariance of the bulk E_A for undoped vs. doped compositions and vs. dopant concentration may indicate three effects: (1) Electrostatic interactions of the dopant and mobile ion that may lower Li mobility do not appear to be dominant. (2) The nominally undoped ($x = 0$) composition may have actually been slightly Li-rich, pushing the E_F below the stoichiometric value (see Fig. 10) and thus favoring $Li_i^\bullet$ formation over vacancies. For a truly stoichiometric undoped sample, one expects E_A to include the defect formation energy as well as the migration (including dissociation) energy, whereas for a doped sample, one expects the defect formation energy term to be absent, since the defect concentration is instead pinned by the dopant concentration and temperature-independent. If the $x = 0$ sample was actually Li-rich, its $Li_i^\bullet$ defect formation energy term would be very small, and the sample would essentially be self-doped already. (3) Concerted ion transport was not triggered by extrinsic doping as additional $Li_i^\bullet$ beyond the intrinsic population were introduced.[25] One explanation may be that Li^+ were able to partially occupy both octahedral and tetrahedral sites in Li_7BiO_6, making the Li^+ sublattice to be in a disordered state intrinsically [72]. Therefore, even if the Li^+ sublattice configuration could be modified further through the introduction of additional $Li_i^\bullet$, it may have limited effect on the conduction mechanism.

Other than bulk (grain) transport properties, there were extra mid-frequency (MF) arcs that reduced the total conductivity for $x \geq 0.075$ at all temperatures measured, whereas the MF feature was not observed above 28 °C for $x \leq 0.05$. In both cases, the MF arcs showed much higher activation energy below 28 °C, which would lead to $Li_{7+x}Bi_{1-x}Zr_xO_6$ having low total conductivity for low temperatures (more discussion on this property can be found in SI Sec. 2.5). Therefore, $Li_{7+x}Bi_{1-x}Zr_xO_6$ might not be ideal for below-room-temperature applications as a Li^+ conductor.

Computationally, Li_7BiO_6 was found to be thermodynamically stable, but only within a limited range of $\Delta\mu_{Li}$. This narrow stability limited the ability to tune the chemical potentials widely across the chemical potential space and maintain phase purity. Moreover, the calculated concentrations of both v_{Li}' and $Li_i^\bullet$ were similarly high at the equilibrium Fermi energy. For those two reasons, simulations would indicate that compositions are restricted to near the stochiometric 7:1:6 ratio for Li:Bi:O. With this reasoning, one expects that the effectiveness of either aliovalent doping (with ionic compensation) or varying the host ion chemical potentials during synthesis is limited to induce significantly off-stochiometric, single-phase compositions. Nevertheless, experimentally it was still found that ~10% of Zr_{Bi}' and $Li_i^\bullet$ could be introduced into Li_7BiO_6. This apparent discrepancy in the computational vs. experimental results may be caused by the introduction of extrinsic dopant, Zr_{Bi}'—the low formation energy of Zr_{Bi}' may make it more dominant acceptor defects than v_{Li}', pinning the equilibrium Fermi energy around lowest energy defects $Li_i^\bullet$ and Zr_{Bi}' (instead of v_{Li}' and $Li_i^\bullet$ in the intrinsic case). In this case, $Li_i^\bullet$ insertion and off-stoichiometry become possible when energetically favorable extrinsic dopants are introduced.

On the other hand, considering the intrinsic defect simulations, the formation energies of v_{Li}' and $Li_i^\bullet$ were low, which is supportive of our initial hypothesis that the "proximal stoichiometry" feature correlates with an abundance of v_{Li}' and $Li_i^\bullet$. The high and almost equal concentrations of both v_{Li}' and $Li_i^\bullet$ correspond to Li Frenkel disorder (Li sublattice disorder), a characteristic generally considered to be beneficial for ionic transport. As a result, as a compound selected by our descriptor filter exhibiting a strong "proximal stoichiometry" characteristic, Li_7BiO_6 was indeed intrinsically Li-defect-rich and disordered. We conclude that the v_{Li}' and $Li_i^\bullet$ defect concentrations would need to be higher to boost the conductivity further and that, under these equilibrium conditions, they may not have been high enough to trigger the concerted hopping mechanism – although the optimal concentration and distribution of Li among sites for concerted transport remains an open question. There are also likely more factors worth considering that could augment our descriptor filters to identify new ionic conductors, which will be discussed in Sec. 4.2.

4.1.2. Defect chemistries/electrical properties of $Li_2B_4O_7$

In Sec. 3.2.2, it was found experimentally that (1) impurity phases form easily with slight variation in Li:B ratio; (2) conductivities were similar in both Li-rich and Li-poor conditions. These results suggest that $Li_2B_4O_7$ was likely a line compound with respect to Li stoichiometry, and the defect concentrations in $Li_2B_4O_7$ did not vary much between Li-rich and Li-poor samples (corresponding to F and E in Fig. 9(b) respectively). The E_A were also similar (and high) in both conditions, indicating that concerted ion transport was likely absent in the system and possibly that the defect formation energy term is contributing to E_A for the intrinsic (stoichiometric) case. The calculated phase stability region also corroborates the experiments. With limited $\Delta\mu_{Li}$, impurity phases form easily, making $Li_2B_4O_7$ essentially a line compound in terms of Li stoichiometry. Therefore, possible improvements in conductivity through overall stoichiometry engineering may be limited, via either adjusting relative chemical potentials during synthesis or extrinsic doping. Furthermore, extrinsic doping can be experimentally challenging because (a) the ionic radii of Li and B are similar and small, making it difficult to find suitable dopants; (b) O substitution is challenging through bulk synthesis.

Considering intrinsic defects, on the other hand, the defect calculations did again show that the formation energies of v_{Li}' and $Li_i^\bullet$ were the lowest among all relevant point defect types, indicating that the correlation between "proximal stoichiometry" and desirable Li Frenkel disorder was also present. However, the formation energies of v_{Li}' and $Li_i^\bullet$ were not particularly low, and so their concentrations were low at the temperatures studied. This is also consistent with experimentally lower

conductivity of $Li_2B_4O_7$. These results suggest that one should also consider strategies for finding even lower formation energies for both v_{Li}' and $Li_i^{\bullet}$, in addition to them being the easiest to form among all defects; more details on this point will be discussed in Sec. 4.2. Furthermore, although more expensive, it may be worth exploring defect chemistries (specifically the v_{Li}' and $Li_i^{\bullet}$ formation energies) computationally first, as a final filtering step, before experimental efforts in future work.

4.2. Implication of proximal stoichiometry filter

The chemical potential spaces and defect calculation diagrams of Li_7BiO_6 and $Li_2B_4O_7$ had the following similarities:

1. The stability regions for Li_7BiO_6 and $Li_2B_4O_7$ were narrow and "stick-like" in shape, due to many nearby competing phases cutting through the chemical potential space. Thus, the tunability of $\Delta\mu_{Li}$ is limited; further variation of $\Delta\mu_{Li}$ would lead to competing phases being more thermodynamically favorable.
2. Li^+ interstitials and vacancies were the most favorable amongst all possible point defects, forming a small tent-like shape in the plot of defect concentration vs. Fermi level, with its peak near the equilibrium Fermi energy.

The above observations are supportive of a correlation between a "proximal stoichiometry" descriptor and easier Li^+ interstitial and vacancy formation. Compositions satisfying the descriptor also tend to have similar v_{Li}' and $Li_i^{\bullet}$ concentrations, corresponding to Li Frenkel disorder. On the one hand, the proximal phase feature therefore constrains the stoichiometry and may thereby limit asymmetric v_{Li}' and $Li_i^{\bullet}$ populations via extrinsic doping, intentional introduction of off-stoichiometry via starting reagent ratios, or modifying gas-phase chemical potentials during synthesis. However, on the other hand, having limited tunability of $\Delta\mu_{Li}$ is not necessarily detrimental for defect formation or transport, since intrinsic disorder that maintains the overall stoichiometry could in principle generate high conductivity if the formation energies are low enough and Li mobility high enough.

Existing phase stability/defect chemistry calculations for other SICs also suggest a correlation between the "proximal stoichiometry" feature and high Li^+ vacancy/interstitial concentrations. Several SICs exhibit a narrow and stick-like thermodynamic stability region [71,73–75], similar to those observed in Li_7BiO_6 and $Li_2B_4O_7$ (Fig. 9). Furthermore, Li vacancies and interstitials were reported to be dominant point defects in LLZO [71], Li_6PS_5X (X = Cl, I) [75], and LGPS [73,74] from first-principles defect calculations, their v_{Li}' and $Li_i^{\bullet}$ concentrations were also reported to be in the same magnitude. Many experimental reports also support the formation of Li-related defects in these SICs [1,24]. However, it is worth noting that in some cases, other point defects can also have relatively low formation energies due to complex structures/compositions and close ionic sizes, e.g., La_{Zr}' and $Zr_{La}^{\bullet}$ anti-site defects in LLZO [71], or $P_{Ge}^{\bullet}$ anti-site defects in LGPS [73,74]. Li_3OCl is identified as an outlier that does not have high concentrations for both v_{Li}' and $Li_i^{\bullet}$ [76]—the lowest energy point defects are v_{Li}', v_{Cl}' and O_{Cl}' in Li_3OCl, with the actual conduction mechanism of anti-perovskites still under debate [1,24].

Interestingly, the position of the apex of the "tent" determines the equilibrium Fermi energy around the lateral intersection of v_{Li}' and $Li_i^{\bullet}$, and its height therefore determines the corresponding defect formation energies/concentrations (illustrated in Fig. 11). For LLZO [71], the peak of the tent formed by v_{Li}' and $Li_i^{\bullet}$ is around 0.5 eV, leading to net Li defect concentrations between 10^{17} to 10^{18} cm^{-3} at a representative synthesis temperature of 1500 K. For LGPS, the intersection points are at approximately 0.20–0.25 eV, implying the abundance of Li defects and Li sublattice disorder in the structure. The estimated defect concentrations of $Li_i^{\bullet}$ in LGPS [74] span from 9×10^{19} to 4×10^{20} cm^{-3} at synthesis temperature 823 K.

While Li^+ interstitials and vacancies were the most abundant defects, the conductivities of Li_7BiO_6 and $Li_2B_4O_7$ were still lower than those of the best SICs; their E_A is also relatively high. One likely reason for this difference may be due to defect concentrations of v_{Li}' and $Li_i^{\bullet}$ not being sufficiently high, with the apex of the tent not being at low enough formation energies (Eq. (4)). A lower tent apex, where v_{Li}' and $Li_i^{\bullet}$ concentration lines intersect, can effectively enhance concentrations for both defects and promote Li^+ sublattice disorder (illustrated in Fig. 11). On the other hand, the apparent E_A measured is a summation of both defect migration energy and formation energies in the intrinsic case. As a result, further lowering the formation energies of both v_{Li}' and $Li_i^{\bullet}$ at the equilibrium Fermi energy may be an important additional filter criterion to design new compositions with high ionic conductivities — beneficial for both increasing defect concentrations and lowering E_A. Therefore, we propose that an improved route to identify SICs is to find candidates with both the "proximal stoichiometry" characteristic and a "low tent" feature in defect diagrams, where the latter step would be the final (most computationally expensive) filter applied to the least number of compounds. However, it is still unclear how to design materials with low defect formation energies for certain defects at equilibrium Fermi

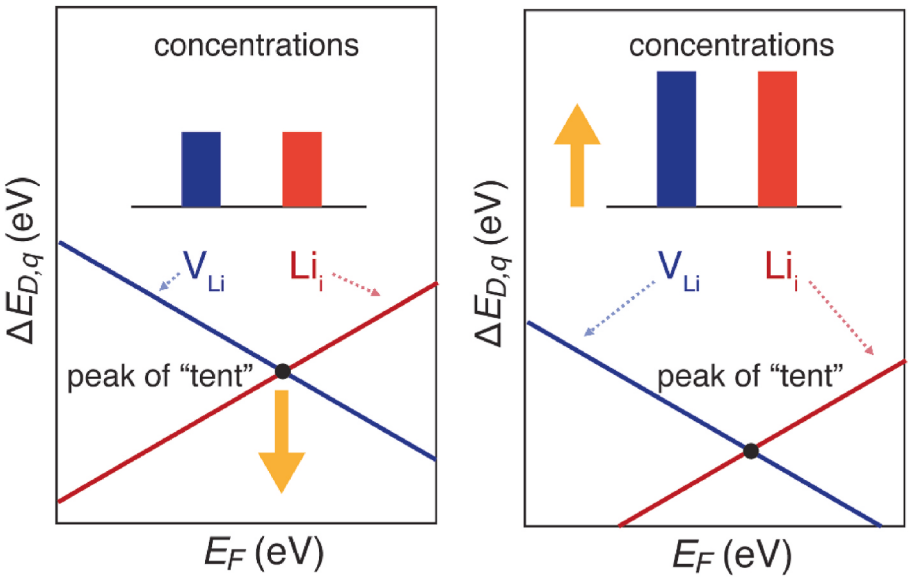

Fig. 11. Illustration of formation energies ($\Delta E_{D,q}$) of v_{Li}' and $Li_i^{\bullet}$ as a function of Fermi energy (E_F). The intersection of v_{Li}' and $Li_i^{\bullet}$, or peak of "tent", determines their formation energies around equilibrium Fermi energy. If the height of peak of "tent" can be lowered, the formation energies of v_{Li}' and $Li_i^{\bullet}$ at equilibrium Fermi energy decrease, leading to higher concentrations of v_{Li}' and $Li_i^{\bullet}$. As a result, a low peak of "tent" can lead to a high concentration of Frenkel defect, and promotes Li^+ sublattice disorder to improve conductivity.

energy, in other words what the descriptor proxy may be to speed up that stage of filtering.

Taken together, the "proximal stoichiometry" feature can be viewed as a double-edged sword in terms of identifying compounds suitable for ionic conductors from our observation in Li_7BiO_6, $Li_2B_4O_7$ and several SICs [71,73–75]. On one hand, it helps to find compounds with coordination flexibility, and therefore supports the formation of intrinsic Frenkel defects. On the other hand, it also leads to narrow stability regions, due to nearby competing phases, which could make it challenging for the introduction of extrinsic carriers. Relating back to our initial hypotheses, our findings are supportive of the first part of our initial hypothesis: there is some correlation between the "proximal stoichiometry" feature and Li^+ sublattice disorder and defect formation. Considering that MP is a materials database that does not include defect thermodynamic data, the ability of this new MP-based proxy/descriptor to predict compounds with favorably low Li Frenkel defect formation energies is significant. However, Li_7BiO_6 and $Li_2B_4O_7$ did not satisfy the second part of the hypothesis: concerted transport was not intentionally triggered in them — either because the increased presence of Li^+ interstitials did not initiate this transport mechanism (Li_7BiO_6) or because significant Li non-stoichiometry could not be introduced ($Li_2B_4O_7$).

Although there were still many untested compositions from our screening results that could be interesting for future experimental/computational work, our results still suggest that additional filtering criteria may be required to identify compositions with the easier defect formation and the potential for concerted transport mechanism:

a) Is there a method to quickly identify compositions with lower height for the "tent" apex in defect diagrams to ensure even lower formation energies?
b) An intermediate criterion of $E_{m,BV} < 1$ eV was used in this work; a stricter constraint or more accurate measure/predictor of migration energy may be needed.
c) Occupancy of both high- and low-energy Li^+ sites was theorized to be beneficial for inducing the concerted transport mechanism [25]. It may be worthwhile to contemplate (1) more specifically what are the descriptive features of the desired distribution of Li in 4D space-energy coordinates, and (2) how might this distribution be encoded using, e.g., pymatgen for screening large databases, as calculations of potential unoccupied high energy sites are computationally expensive.
d) $CN_{Li–Li}$ was used as a descriptor in this work to approximate some sense of Li–Li interactions, although Li–Li distances were also calculated and considered. Could these other criteria such as Li–Li distance or Li^+ 3D density better capture Li–Li interactions, to serve as high-throughput-suitable fingerprints for likely concerted transport?

In addition to finding electrolytes, the "proximal stoichiometry" descriptor may be of interest for identifying new electrode materials in the future. Although the $\Delta\mu_{Li}$ of each phase may be limited, these phase diagrams indicate a series of stable phases at closely-spaced varying Li chemical potentials, as would occur during lithiation/delithiation, and many electrode materials undergo/rely on phase transitions during charging/discharging [77–79]. In order to find electrode materials, certain steps in the filtering process would need adjusting. For instance, since electronic conductivity is desirable in this case, one can relax the large bandgap criterion and re-allow inclusion of transition metals, where the latter may also facilitate redox reactions.

5. Summary and conclusion

In this work, we hypothesized that the "proximal stoichiometry" feature may be used as a computationally inexpensive proxy for identifying compositions supporting Li^+ sublattice disorder through the formation of Frenkel defects. These compositions may have potential in application as solid electrolyte materials, as the ability to accommodate Li^+ defects and disorder is crucial for promoting ionic conduction.

To test out this hypothesis, a series of descriptors based on "proximal stoichiometry," bond valence migration energy, Li–Li coordination number, etc., were designed. Using Materials Project as the initial database, the compositions were down-selected in a high-throughput fashion. After preliminary screening, it was found that many SICs possess this "proximal stoichiometry" feature, with low formation energies of v_{Li}' and $Li_i^{\bullet}$. This finding indicated that our new descriptor is correlated to the ability to host Li defects and create Li^+ sublattice disorder, and new compositions sharing the same characteristic could also have high ionic conductivity.

From the complete, sequential descriptor filtering process, Li_7BiO_6 and $Li_2B_4O_7$ were selected as candidates for in-depth computational/experimental investigations. It was found computationally that they were indeed Li-defect-rich with the formation of Frenkel defects, but their tunabilities in $\Delta\mu_{Li}$ were limited. Other SICs with "proximal stoichiometry" feature also showed such similarities in terms of phase stability and defect formation. Experimentally, Li^+ insertion was attempted on Li_7BiO_6, where Zr^{4+} was substituted on Bi^{5+} sites to compensate for Li^+ interstitials. It was found that up to 10% of $Li_i^{\bullet}$ and Zr_{Bi}' could be introduced, but the conductivity only improved for $Li_{7.05}Bi_{0.95}Zr_{0.05}O_6$. Although Li_7BiO_6 can accommodate Li^+ interstitials to some degree, the improvement in conductivity is limited with unchanged E_A, and concerted ion transport could not be triggered over the experimentally studied range of $\Delta\mu_{Li}$. On the other hand, $Li_2B_4O_7$ was found to be a line compound, and the conductivity and E_A did not change much in Li-rich and Li-poor conditions.

In summary, our findings support that there is a correlation between the "proximal stoichiometry" feature and the ability to accommodate Li disorder in the form of interstitials and vacancies with low formation energies. However, the correlation between the ability to accommodate disorder/defects and concerted ion transport may not be straightforward, as seen in Li_7BiO_6 and $Li_2B_4O_7$ experimentally. In other words, the "proximal stoichiometry" feature does not necessarily mean that significant improvements in conductivity can be achieved via extrinsic doping or that the intrinsic conductivity is as high as the best SICs. As a result, we have proposed questions and pathways to follow for additional descriptors/proxies that may augment this descriptor filter recipe in future work. These additional features would ideally assist in identification of new compositions with even more favorable Li defect formation energies, with a low peak of the Li interstitial/vacancy "tent" on the defect diagrams, or the potential for concerted ion transport with more suitable Li-sublattice configurations.

CRediT authorship contribution statement

Yu-Ying Lin: Conceptualization, Methodology, Formal analysis, Investigation, Validation, Software, Visualization, Writing – original draft, Writing – review & editing, Project administration. **Jiaxing Qu:** Formal analysis, Software, Visualization, Writing – original draft, Writing – review & editing. **William J. Gustafson:** Formal analysis, Software. **Po-Cheng Kung:** Investigation. **Nachiket Shah:** Investigation. **Samyukta Shrivastav:** Investigation. **Elif Ertekin:** Conceptualization, Resources, Methodology, Supervision, Writing – review & editing, Funding acquisition. **Jessica A. Krogstad:** Conceptualization, Methodology, Resources, Supervision, Writing – review & editing, Project administration, Funding acquisition. **Nicola H. Perry:** Conceptualization, Methodology, Resources, Supervision, Writing – review & editing, Project administration, Funding acquisition.

Declaration of competing interest

The authors declare that they have no known competing financial interests or personal relationships that could have appeared to influence the work reported in this paper.

Data availability

Data will be made available on request.

Acknowledgments

This material is primarily based upon work supported by the US Army CERL W9132T-19-2-0008 and subsequently US Army CERL W9132T-21-2-0008 (both to E.E., J.A.K., and N.H.P., also supporting Y. Y.L.). XRD, SEM, TEM, TGA and sputter coating were carried out in the Materials Research Laboratory Central Research Facilities, University of Illinois. The authors also acknowledge the use of XRD instrumentation supported by NSF through the University of Illinois Materials Research Science and Engineering Center DMR-1720633. J.Q. acknowledges funding from NSF DIGI-MAT program, Grant No. 1922758.

Appendix A. Supplementary data

Supplementary data to this article can be found online at https://doi.org/10.1016/j.jpowsour.2022.232251.

References

[1] Z. Zhang, Y. Shao, B. Lotsch, Y.-S.S. Hu, H. Li, J. Janek, L.F. Nazar, C.-W.W. Nan, J. Maier, M. Armand, L. Chen, New horizons for inorganic solid state ion conductors, Energy Environ. Sci. 11 (2018) 1945–1976, https://doi.org/10.1039/c8ee01053f.

[2] S.A. Pervez, M.A. Cambaz, V. Thangadurai, M. Fichtner, Interface in solid-state lithium battery: challenges, progress, and outlook, ACS Appl. Mater. Interfaces 11 (2019) 22029–22050, https://doi.org/10.1021/acsami.9b02675.

[3] Y. Xiao, K. Jun, Y. Wang, L.J. Miara, Q. Tu, G. Ceder, Lithium oxide superionic conductors inspired by garnet and NASICON structures, Adv. Energy Mater. 11 (2021), 2101437, https://doi.org/10.1002/aenm.202101437.

[4] Y. Inoue, K. Suzuki, N. Matsui, M. Hirayama, R. Kanno, Synthesis and structure of novel lithium-ion conductor Li7Ge3PS12, J. Solid State Chem. 246 (2017) 334–340, https://doi.org/10.1016/j.jssc.2016.12.001.

[5] H.Y.-P. Hong, Crystal structure and ionic conductivity of Li14Zn(GeO4)4 and other new Li+ superionic conductors, Mater. Res. Bull. 13 (1978) 117–124, https://doi.org/10.1016/0025-5408(78)90075-2.

[6] V. Thangadurai, W. Weppner, Li6ALa2Nb2O12 (A=Ca, Sr, Ba): a new class of fast lithium ion conductors with garnet-like structure, J. Am. Ceram. Soc. 88 (2005) 411–418, https://doi.org/10.1111/j.1551-2916.2005.00060.x.

[7] Y. Xiao, K. Jun, Y. Wang, L.J. Miara, Q. Tu, G. Ceder, Lithium oxide superionic conductors inspired by garnet and NASICON structures, Adv. Energy Mater. 11 (2021), 2101437, https://doi.org/10.1002/aenm.202101437.

[8] Y.-Y. Lin, W.J. Gustafson, S.E. Murray, D.P. Shoemaker, E. Ertekin, J.A. Krogstad, N.H. Perry, Perovskite Na-ion conductors developed from analogous Li3xLa2/3-xTiO3 (LLTO): chemo-mechanical and defect engineering, J Mater Chem A Mater 9 (2021) 21241–21258, https://doi.org/10.1039/D1TA04252A.

[9] X. He, Q. Bai, Y. Liu, A.M. Nolan, C. Ling, Y. Mo, Crystal structural framework of lithium super-ionic conductors, Adv. Energy Mater. 9 (2019), 1902078, https://doi.org/10.1002/aenm.201902078.

[10] Z. Xu, H. Zhu, Anion charge and lattice volume maps for searching lithium superionic conductors, Chem. Mater. 32 (2020) 4618–4626, https://doi.org/10.1021/acs.chemmater.0c00993.

[11] Z. Xu, X. Chen, R. Chen, X. Li, H. Zhu, Anion charge and lattice volume dependent lithium ion migration in compounds with fcc anion sublattices, NPJ Comput Mater 6 (2020) 47, https://doi.org/10.1038/s41524-020-0324-7.

[12] N.A. Katcho, J. Carrete, M. Reynaud, G. Rousse, M. Casas-Cabanas, N. Mingo, J. Rodríguez-Carvajal, J. Carrasco, An investigation of the structural properties of Li and Na fast ion conductors using high-throughput bond-valence calculations and machine learning, J. Appl. Crystallogr. 52 (2019) 148–157, https://doi.org/10.1107/S1600576718018484.

[13] A.D. Sendek, Q. Yang, E.D. Cubuk, K.A.N. Duerloo, Y. Cui, E.J. Reed, Holistic computational structure screening of more than 12 000 candidates for solid lithium-ion conductor materials, Energy Environ. Sci. 10 (2017) 306–320, https://doi.org/10.1039/c6ee02697d.

[14] Y. Zhang, X. He, Z. Chen, Q. Bai, A.M. Nolan, C.A. Roberts, D. Banerjee, T. Matsunaga, Y. Mo, C. Ling, Unsupervised discovery of solid-state lithium ion conductors, Nat. Commun. 10 (2019) 5260, https://doi.org/10.1038/s41467-019-13214-1.

[15] E.D. Cubuk, A.D. Sendek, E.J. Reed, Screening billions of candidates for solid lithium-ion conductors: a transfer learning approach for small data, J. Chem. Phys. 150 (2019), 214701, https://doi.org/10.1063/1.5093220.

[16] B. Kozinsky, S.A. Akhade, P. Hirel, A. Hashibon, C. Elsässer, P. Mehta, A. Logeat, U. Eisele, Effects of sublattice symmetry and frustration on ionic transport in garnet solid electrolytes, Phys. Rev. Lett. 116 (2016), 055901, https://doi.org/10.1103/PhysRevLett.116.055901.

[17] R. Jalem, Y. Yamamoto, H. Shiiba, M. Nakayama, H. Munakata, T. Kasuga, K. Kanamura, Concerted migration mechanism in the Li ion dynamics of garnet-type $Li_7La_3Zr_2O_{12}$, Chem. Mater. 25 (2013) 425–430, https://doi.org/10.1021/cm303542x.

[18] D.A. Keen, A.L. Goodwin, The crystallography of correlated disorder, Nature 521 (2015) 303–309, https://doi.org/10.1038/nature14453.

[19] K. Fujimura, A. Seko, Y. Koyama, A. Kuwabara, I. Kishida, K. Shitara, C.A.J. Fisher, H. Moriwake, I. Tanaka, Accelerated materials design of lithium superionic conductors based on first-principles calculations and machine learning algorithms, Adv. Energy Mater. 3 (2013) 980–985, https://doi.org/10.1002/aenm.201300060.

[20] G.K. Phani Dathar, J. Balachandran, P.R.C. Kent, A.J. Rondinone, P. Ganesh, Li-ion site disorder driven superionic conductivity in solid electrolytes: a first-principles investigation of β-Li3PS4, J Mater Chem A Mater 5 (2017) 1153–1159, https://doi.org/10.1039/C6TA07713G.

[21] Y. Sun, P. Guan, Y. Liu, H. Xu, S. Li, D. Chu, Recent progress in lithium lanthanum titanate electrolyte towards all solid-state lithium ion secondary battery, Crit. Rev. Solid State Mater. Sci. 44 (2019) 265–282, https://doi.org/10.1080/10408436.2018.1485551.

[22] B. Kozinsky, Transport in frustrated and disordered solid electrolytes, in: Handbook of Materials Modeling, Springer International Publishing, Cham, 2018, pp. 1–20, https://doi.org/10.1007/978-3-319-50257-1_54-1.

[23] Y. Deng, C. Eames, B. Fleutot, R. David, J.-N. Chotard, E. Suard, C. Masquelier, M. S. Islam, Enhancing the lithium ion conductivity in lithium superionic conductor (LISICON) solid electrolytes through a mixed polyanion effect, ACS Appl. Mater. Interfaces 9 (2017) 7050–7058, https://doi.org/10.1021/acsami.6b14402.

[24] Y.-Y. Lin, A.X. bin Yong, W.J. Gustafson, C.N. Reedy, E. Ertekin, J.A. Krogstad, N. H. Perry, Toward design of cation transport in solid-state battery electrolytes: structure-dynamics relationships, Curr. Opin. Solid State Mater. Sci. 24 (2020), 100875, https://doi.org/10.1016/j.cossms.2020.100875.

[25] X. He, Y. Zhu, Y. Mo, Origin of fast ion diffusion in super-ionic conductors, Nat. Commun. 8 (2017), 15893, https://doi.org/10.1038/ncomms15893.

[26] M. Catti, Short-range order and Li+ ion diffusion mechanisms in Li5La9□2(TiO3) 16 (LLTO), Solid State Ionics 183 (2011) 1–6, https://doi.org/10.1016/j.ssi.2010.12.016.

[27] A. Kežionis, E. Kazakevičius, S. Kazlauskas, A. Žalga, Metal-like temperature dependent conductivity in fast Li^+ ionic conductor Lithium Lanthanum Titanate, Solid State Ionics 342 (2019), 115060, https://doi.org/10.1016/j.ssi.2019.115060.

[28] Y. Deng, C. Eames, J.-N. Chotard, F. Lalère, V. Seznec, S. Emge, O. Pecher, C. P. Grey, C. Masquelier, M.S. Islam, Structural and mechanistic insights into fast lithium-ion conduction in Li4SiO4-Li3PO4 solid electrolytes, J. Am. Chem. Soc. 137 (2015) 9136–9145, https://doi.org/10.1021/jacs.5b04444.

[29] Y.A. Du, N.A.W. Holzwarth, Li ion diffusion mechanisms in the crystalline electrolyte γ-Li_3PO_4, J. Electrochem. Soc. 154 (2007) A999, https://doi.org/10.1149/1.2772200.

[30] X. Lu, S. Wang, R. Xiao, S. Shi, H. Li, L. Chen, First-principles insight into the structural fundamental of super ionic conducting in NASICON $MTi_2(PO_4)_3$ (M = Li, Na) materials for rechargeable batteries, Nano Energy 41 (2017) 626–633, https://doi.org/10.1016/j.nanoen.2017.09.044.

[31] Z. Zhang, Z. Zou, K. Kaup, R. Xiao, S. Shi, M. Avdeev, Y.S. Hu, D. Wang, B. He, H. Li, X. Huang, L.F. Nazar, L. Chen, Correlated migration invokes higher Na^+-Ion conductivity in NaSICON-type solid electrolytes, Adv. Energy Mater. 9 (2019) 1–14, https://doi.org/10.1002/aenm.201902373.

[32] B. Zhang, Z. Lin, H. Dong, L.-W. Wang, F. Pan, Revealing cooperative Li-ion migration in $Li_{1+x}Al_xTi_{2-x}(PO_4)_3$ solid state electrolytes with high Al doping, J Mater Chem A Mater 8 (2020) 342–348, https://doi.org/10.1039/C9TA09770H.

[33] S. Xiong, X. He, A. Han, Z. Liu, Z. Ren, B. McElhenny, A.M. Nolan, S. Chen, Y. Mo, H. Chen, Computation-guided design of LiTaSiO5, a new lithium ionic conductor with sphene structure, Adv. Energy Mater. (2019), https://doi.org/10.1002/aenm.201803821.

[34] Z. Zou, N. Ma, A. Wang, Y. Ran, T. Song, Y. Jiao, J. Liu, H. Zhou, W. Shi, B. He, D. Wang, Y. Li, M. Avdeev, S. Shi, Relationships between Na + distribution, concerted migration, and diffusion properties in rhombohedral NASICON, Adv. Energy Mater. (2020), 2001486, https://doi.org/10.1002/aenm.202001486.

[35] A. Jain, S.P. Ong, G. Hautier, W. Chen, W.D. Richards, S. Dacek, S. Cholia, D. Gunter, D. Skinner, G. Ceder, K.A. Persson, Commentary: the Materials Project: a materials genome approach to accelerating materials innovation, Apl. Mater. 1 (2013), 011002, https://doi.org/10.1063/1.4812323.

[36] S. Adams, R.P. Rao, Transport pathways for mobile ions in disordered solids from the analysis of energy-scaled bond-valence mismatch landscapes, Phys. Chem. Chem. Phys. 11 (2009) 3210, https://doi.org/10.1039/b901753d.

[37] S. Adams, Bond valence analysis of structure-property relationships in solid electrolytes, J. Power Sources 159 (2006) 200–204, https://doi.org/10.1016/j.jpowsour.2006.04.085.

[38] R. Xiao, H. Li, L. Chen, High-throughput design and optimization of fast lithium ion conductors by the combination of bond-valence method and density functional theory, Sci. Rep. 5 (2015) 1–11, https://doi.org/10.1038/srep14227.

[39] J. Rodríguez-Carvajal, Recent advances in magnetic structure determination by neutron powder diffraction, Phys. B Condens. Matter 192 (1993) 55–69, https://doi.org/10.1016/0921-4526(93)90108-I.

[40] M. Anilkumar, R. Pasricha, V. Ravi, Synthesis of bismuth oxide nanoparticles by citrate gel method, Ceram. Int. 31 (2005) 889–891, https://doi.org/10.1016/j.ceramint.2004.09.002.

[41] J.F.M. J, N. A, S. S, Improved carrier mobility and bandgap tuning of zinc doped bismuth oxide, RSC Adv. 5 (2015) 2504–2510, https://doi.org/10.1039/C4RA12494D.

[42] S. Gates-Rector, T. Blanton, The Powder Diffraction File: a quality materials characterization database, Powder Diffr. 34 (2019) 352–360, https://doi.org/10.1017/S0885715619000812.
[43] T.H. Wan, M. Saccoccio, C. Chen, F. Ciucci, Influence of the discretization methods on the distribution of relaxation times deconvolution: implementing radial basis functions with DRTtools, Electrochim. Acta 184 (2015) 483–499, https://doi.org/10.1016/j.electacta.2015.09.097.
[44] D.A.G. Bruggeman, Berechnung verschiedener physikalischer Konstanten von heterogenen Substanzen. I. Dielektrizitätskonstanten und Leitfähigkeiten der Mischkörper aus isotropen Substanzen, Ann. Phys. 416 (1935) 636–664, https://doi.org/10.1002/andp.19354160705.
[45] D.S. McLachlan, M. Blaszkiewicz, R.E. Newnham, Electrical resistivity of composites, J. Am. Ceram. Soc. 73 (1990) 2187–2203, https://doi.org/10.1111/j.1151-2916.1990.tb07576.x.
[46] W. Pabst, E. Gregorová, Conductivity of porous materials with spheroidal pores, J. Eur. Ceram. Soc. 34 (2014) 2757–2766, https://doi.org/10.1016/j.jeurceramsoc.2013.12.040.
[47] A.S. Botana, M.R. Norman, Electronic structure and magnetism of transition metal dihalides: bulk to monolayer, Phys Rev Mater 3 (2019), 44001, https://doi.org/10.1103/PhysRevMaterials.3.044001.
[48] J. Tao, J.P. Perdew, H. Tang, C. Shahi, Origin of the size-dependence of the equilibrium van der Waals binding between nanostructures, J. Chem. Phys. 148 (2018), 074110, https://doi.org/10.1063/1.5018572.
[49] P.E. Blöchl, O. Jepsen, O.K. Andersen, Improved tetrahedron method for Brillouin-zone integrations, Phys. Rev. B 49 (1994) 16223–16233, https://doi.org/10.1103/PhysRevB.49.16223.
[50] A. Belsky, M. Hellenbrandt, V.L. Karen, P. Luksch, New developments in the Inorganic Crystal Structure Database (ICSD): accessibility in support of materials research and design, Acta Crystallogr. B 58 (2002) 364–369, https://doi.org/10.1107/S0108768102006948.
[51] P.J. Linstrom, W.G. Mallard, The nist chemistry WebBook: a chemical data resource on the internet, J. Chem. Eng. Data 46 (2001) 1059–1063, https://doi.org/10.1021/je000236i.
[52] S. Lany, A. Zunger, Assessment of correction methods for the band-gap problem and for finite-size effects in supercell defect calculations: case studies for ZnO and GaAs, Phys. Rev. B 78 (2008), 235104, https://doi.org/10.1103/PhysRevB.78.235104.
[53] S. Baroni, S. de Gironcoli, A. Dal Corso, P. Giannozzi, Phonons and related crystal properties from density-functional perturbation theory, Rev. Mod. Phys. 73 (2001) 515–562, https://doi.org/10.1103/RevModPhys.73.515.
[54] A. Goyal, P. Gorai, E.S. Toberer, V. Stevanović, First-principles calculation of intrinsic defect chemistry and self-doping in PbTe, NPJ Comput Mater 3 (2017) 42, https://doi.org/10.1038/s41524-017-0047-6.
[55] V. Stevanović, S. Lany, X. Zhang, A. Zunger, Correcting density functional theory for accurate predictions of compound enthalpies of formation: fitted elemental-phase reference energies, Phys. Rev. B 85 (2012), 115104, https://doi.org/10.1103/PhysRevB.85.115104.
[56] M. Wilkening, C. Mühle, M. Jansen, P. Heitjans, Microscopic access to long-range diffusion parameters of the fast lithium ion conductor Li 7 BiO 6 by solid state 7 Li stimulated echo NMR, J. Phys. Chem. B 111 (2007) 8691–8694, https://doi.org/10.1021/jp0734979.
[57] C. V Subban, G. Rousse, R.-N. Vannier, C. Laberty-Robert, P. Barboux, J.-M. Tarascon, Search for Li-electrochemical activity and Li-ion conductivity among lithium bismuth oxides, Solid State Ionics 283 (2015) 68–74, https://doi.org/10.1016/j.ssi.2015.10.016.
[58] E. Nomura, M. Greenblatt, Ionic conductivity of Li7BiO6, J. Solid State Chem. (1984), https://doi.org/10.1016/0022-4596(84)90202-0.
[59] C. Mühle, A. Karpov, A. Verhoeven, M. Jansen, Crystal structures, dimorphism and lithium mobility of Li7MO6 (M = Bi, Ru, Os), Z. Anorg. Allg. Chem. 631 (2005) 2321–2327, https://doi.org/10.1002/zaac.200500231.
[60] C. Mühle, R.E. Dinnebier, L. van Wüllen, G. Schwering, M. Jansen, New insights into the structural and dynamical features of lithium hexaoxometalates Li 7 MO 6 (M = Nb, Ta, Sb, Bi), Inorg. Chem. 43 (2004) 874–881, https://doi.org/10.1021/ic030208w.
[61] C.-S. Kim, D.J. Kim, Y.-H. Hwang, H.K. Kim, J.N. Kim, Electrical properties of Li2B4O7 single crystals in the [001] direction: comparison between crystals grown from Li2CO3 and B2O3 mixed powder and from Li2B4O7 powder, J. Appl. Phys. 92 (2002) 4644–4648, https://doi.org/10.1063/1.1505980.
[62] M.M. Islam, T. Bredow, C. Minot, Ionic conductivity of Li 2 B 4 O 7, J. Phys. Chem. B 110 (2006) 17518–17523, https://doi.org/10.1021/jp061785j.
[63] T.D. Kelly, L. Kong, D.A. Buchanan, A.T. Brant, J.C. Petrosky, J.W. McClory, V. T. Adamiv, Y. v Burak, P.A. Dowben, EXAFS and EPR analysis of the local structure of Mn-doped Li2B4O7, Phys. Status Solidi 250 (2013) 1376–1383, https://doi.org/10.1002/pssb.201349013.
[64] T. Aydın, H. Demirtaş, S. Aydın, TL/OSL studies of Li2B4O7:Cu dosimetric phosphors, Radiat. Meas. 58 (2013) 24–32, https://doi.org/10.1016/j.radmeas.2013.07.010.
[65] B.A. Doull, L.C. Oliveira, E.G. Yukihara, Effect of annealing and fuel type on the thermoluminescent properties of Li2B4O7 synthesized by Solution Combustion Synthesis, Radiat. Meas. 56 (2013) 167–170, https://doi.org/10.1016/j.radmeas.2013.02.003.
[66] C.B. Palan, A.O. Chauhan, N.S. Sawala, N.S. Bajaj, S.K. Omanwar, Synthesis and preliminary TL/OSL properties of Li2B4O7: Cu-Ag phosphor for radiation dosimetry, Optik 127 (2016) 6419–6423, https://doi.org/10.1016/j.ijleo.2016.04.128.
[67] L. Fan, Z. Liu, Y. Zhu, Z. Wang, S. Zhao, L. Zhu, Q. Zhang, Synthesis of Li-doping tetragonal-Bi2O3 nanomaterial with high efficient visible light photocatalysis, J. Mater. Sci. Mater. Electron. 31 (2020) 2100–2110, https://doi.org/10.1007/s10854-019-02731-w.
[68] M.G. Celik, A. Yilmaz, A.N. Yazici, Synthesis and thermoluminescence characterization of lithium tetraborate (Li2B4O7) doped with copper and silver metals, Radiat. Meas. 102 (2017) 16–26, https://doi.org/10.1016/j.radmeas.2017.06.002.
[69] P. Heitjans, E. Tobschall, M. Wilkening, Ion transport and diffusion in nanocrystalline and glassy ceramics, Eur. Phys. J. Spec. Top. 161 (2008) 97–108, https://doi.org/10.1140/epjst/e2008-00753-4.
[70] D. Wohlmuth, V. Epp, B. Stanje, A.-M. Welsch, H. Behrens, M. Wilkening, High-energy mechanical treatment boosts ion transport in nanocrystalline Li2B4O7, J. Am. Ceram. Soc. 99 (2016) 1687–1693, https://doi.org/10.1111/jace.14165.
[71] A.G. Squires, D.O. Scanlon, B.J. Morgan, Native defects and their doping response in the lithium solid electrolyte Li7La3Zr2O12, Chem. Mater. 32 (2020) 1876–1886, https://doi.org/10.1021/acs.chemmater.9b04319.
[72] C. Mühle, R.E. Dinnebier, L. van Wüllen, G. Schwering, M. Jansen, New insights into the structural and dynamical features of lithium hexaoxometalates Li 7 MO 6 (M = Nb, Ta, Sb, Bi), Inorg. Chem. 43 (2004) 874–881, https://doi.org/10.1021/ic030208w.
[73] K. Oh, D. Chang, B. Lee, D.-H. Kim, G. Yoon, I. Park, B. Kim, K. Kang, Native defects in Li10GeP2S12 and their effect on lithium diffusion, Chem. Mater. 30 (2018) 4995–5004, https://doi.org/10.1021/acs.chemmater.8b01163.
[74] P. Gorai, H. Long, E. Jones, S. Santhanagopalan, V. Stevanović, Defect chemistry of disordered solid-state electrolyte $Li_{10}GeP_2S_{12}$, J Mater Chem A Mater 8 (2020) 3851–3858, https://doi.org/10.1039/C9TA10964A.
[75] P. Gorai, T. Famprikis, B. Singh, V. Stevanović, P. Canepa, Devil is in the defects: electronic conductivity in solid electrolytes, Chem. Mater. 33 (2021) 7484–7498, https://doi.org/10.1021/acs.chemmater.1c02345.
[76] A. Squires, J.M. Dean, B.J. Morgan, Aliovalent Doping Response and Impact on Ionic Conductivity in the Antiperovskite Solid Electrolyte Li3OCl, ChemRxiv, 2021.
[77] Y. Lyu, X. Wu, K. Wang, Z. Feng, T. Cheng, Y. Liu, M. Wang, R. Chen, L. Xu, J. Zhou, Y. Lu, B. Guo, An overview on the advances of LiCoO2 cathodes for lithium-ion batteries, Adv. Energy Mater. 11 (2021), 2000982, https://doi.org/10.1002/aenm.202000982.
[78] X.Y. Tu, K.Y. Shu, X-ray diffraction study on phase transition of orthorhombic LiMnO2 in electrochemical conversions, J. Solid State Electrochem. 12 (2008) 245–249, https://doi.org/10.1007/s10008-007-0384-3.
[79] M.G. Verde, L. Baggetto, N. Balke, G.M. Veith, J.K. Seo, Z. Wang, Y.S. Meng, Elucidating the phase transformation of Li4Ti5O12 lithiation at the nanoscale, ACS Nano 10 (2016) 4312–4321, https://doi.org/10.1021/acsnano.5b07875.